

Review

# Vanadium Oxide–Conducting Polymers Composite Cathodes for Aqueous Zinc-Ion Batteries: Interfacial Design and Enhancement of Electrochemical Performance

Elena G. Tolstopyatova <sup>\*</sup>, Mikhail A. Kamenskii  and Veniamin V. Kondratiev

Institute of Chemistry, Saint Petersburg State University, 7/9 Universitetskaya Nab., 199034 Saint Petersburg, Russia  
<sup>\*</sup> Correspondence: e.tolstopyatova@spbu.ru

**Abstract:** Aqueous zinc-ion batteries (AZIBs) are being intensively developed as potential alternative electrochemical power sources, due to their advantages such as low cost, high safety, abundance of natural zinc resources and appropriate energy density. Among currently investigated prospective cathode materials for AZIBs, vanadium oxide-based composites with intrinsically conducting polymers have shown many advantages, such as high capacity, high power density and long battery life. This review gives a focused view of the design for the boosting of zinc ion storage performance using intrinsically conducting polymers in vanadium oxide-based composites and the mechanism of intercalation processes. The main challenges in interfacial engineering of vanadium oxide-conducting polymers composite structures and the prospects for further development of such cathode materials are summarized and discussed. The review would give rise to a broad interest focusing on the advantageous strategy of the development of vanadium oxide composite cathodes with intrinsically conducting polymers (polyaniline, polypyrrole, poly(3,4-ethylenedioxythiophene)) for AZIBs with improved energy density, high-rate capability and stability.

**Keywords:** aqueous zinc-ion battery; vanadium(V) oxide; poly(3,4-ethylenedioxythiophene); polyaniline; polypyrrole; composite cathode; energy storage; electrochemical performance



**Citation:** Tolstopyatova, E.G.; Kamenskii, M.A.; Kondratiev, V.V. Vanadium Oxide–Conducting Polymers Composite Cathodes for Aqueous Zinc-Ion Batteries: Interfacial Design and Enhancement of Electrochemical Performance.

*Energies* **2022**, *15*, 8966. <https://doi.org/10.3390/en15238966>

Academic Editors: Abdal-Ghani Olabi, Michele Dassisi and Zhien Zhang

Received: 29 October 2022

Accepted: 23 November 2022

Published: 27 November 2022

**Publisher's Note:** MDPI stays neutral with regard to jurisdictional claims in published maps and institutional affiliations.



**Copyright:** © 2022 by the authors. Licensee MDPI, Basel, Switzerland. This article is an open access article distributed under the terms and conditions of the Creative Commons Attribution (CC BY) license (<https://creativecommons.org/licenses/by/4.0/>).

## 1. Introduction

In the past few decades, Li-ion batteries have been extensively investigated and commercialized. Versatile lightweight rechargeable Li-ion batteries, providing high energy density, have found widespread applications in our everyday life, such as powering mobile devices and electric vehicles. However, renewable and clean energy technologies, such as grid storage, demand stationary batteries of the next generation—low cost, reliable, environmentally friendly, and safe, with long cycle life (>8000 full cycles) and high energy efficiency (>90%). This demand has accelerated the investigations of the so-called “beyond Li-ion” battery technologies: all-solid-state batteries, Na-ion batteries, K-ion batteries and multivalent metal-ion batteries that may be more suitable for mid-/large-scale applications than the Li-ion ones [1–3]. Rechargeable aqueous batteries have been considered promising candidates for large-scale application due to the various advantages of aqueous electrolytes: noncombustibility, high ionic conductivity, easy processing and environmental friendliness. They are among the safest battery systems, making them ideal for grid storage and also for flexible energy storage devices [4]. Compared to other aqueous metal-ion batteries, aqueous zinc-ion batteries (AZIBs) attract special attention because the high theoretical specific capacity (820 mAh·g<sup>−1</sup>) and high volumetric energy density (5854 mAh·cm<sup>−3</sup>) of the metallic Zn anode can to a considerable extent overcome the issues associated with low energy density due to the limited potential window of aqueous media [5,6]. The additional advantages of metallic Zn are its comparatively low redox potential (−0.76 V vs. the standard hydrogen electrode (SHE)), low cost, high stability in aqueous electrolytes and natural abundance.

Nevertheless, designing cathode materials for AZIBs with high specific capacity and stable long-term cycling performance is still a challenge, because  $\text{Zn}^{2+}$  ions, as other multivalent cations, enter into strong electrostatic interactions with the host materials, and cathodes of AZIBs suffer from sluggish  $\text{Zn}^{2+}$  diffusion kinetics in a crystal lattice, resulting in poor rate performance and short cycle life [7,8].

Among the currently investigated cathode materials for AZIBs, vanadium-containing materials occupy a leading position [9–18]. The wide redox range of vanadium ( $\text{V}^{5+} \leftrightarrow \text{V}^{4+} \leftrightarrow \text{V}^{3+}$ ) allows it to fall within the limited thermodynamically stable electrochemical window of an aqueous electrolyte (up to 1.23 V). The structures with sufficient interlayer distances can facilitate reversibility of  $\text{Zn}^{2+}$  insertion/extraction, which promotes the specific capacity of the electrodes. Thus, layered vanadium oxides are materials with promising charge storing capabilities [19].

Of these, vanadium pentoxide  $\text{V}_2\text{O}_5$  has high theoretical capacity (up to  $589 \text{ mA}\cdot\text{h}\cdot\text{g}^{-1}$  per two-electron process) [20] and suitable structure for ion intercalation, making it widely used as a cathode material for rechargeable batteries [9,10,21–28]. However, the fabrication of  $\text{V}_2\text{O}_5$ -based cathodes for AZIBs featuring high reversible capacity and cycle stability meets a number of challenges [29], which can be, in particular, solved by using intrinsically conducting polymers (further denoted as CPs) as components of  $\text{V}_2\text{O}_5$ -based composite cathodes:

(1) Cathode dissolution [30,31]. The dissolution of  $\text{V}_2\text{O}_5$  cathodes in weakly acidic aqueous electrolytes of AZIBs, especially at low current densities ( $<0.5 \text{ C}$ ), reduces the utilization of active material, induces side reactions at the electrode interface, and causes structural degradation and performance degradation. The surface layer of conducting polymer can protect the active material from direct contact with the electrolyte, thus suppressing the interfacial side reactions, and improve cycling performance at low C-rates.

(2) Structural instability. Repeated charge/discharge causes structural degradation of layered  $\text{V}_2\text{O}_5$ , thus inactivating the active phase of electrode materials. The high charge density of zinc ions generates coulombic interactions with the host material during the  $\text{Zn}^{2+}$  intercalation/deintercalation process. Zinc cations are easily bonded with the oxygen anions of the lattice, which leads to sluggish kinetics of the intercalation/deintercalation of  $\text{Zn}^{2+}$ , decreased capacity and structural damage. Pre-insertion of conducting polymer molecules as the so-called “pillars” to produce materials with permanently expanded interlayer distance can effectively improve stability issues by sustaining the framework [32–37]. Moreover, due to the multivalent nature of the intercalated metal cation, the active material undergoes dramatic volume changes. Conducting polymers may help maintain the cathode integrity and ensure a stable charge–discharge process [38].

(3) Low conductivity. Pristine  $\text{V}_2\text{O}_5$  powder has relatively low electrical conductivity, which results in sluggish reaction kinetics, poor rate performance and a long activation period. The conductivity can be improved by structural engineering of the active material (e.g., introducing metal ions or organic molecules as pillars into layered structures of vanadium oxides) or by surface modification (coating by conducting material with a formation of core-shell structures or hybridizing active materials with a carbon matrix). The use of CPs can significantly increase the electronic and ionic conductivity of composite materials and improve the diffusion kinetics of zinc ions inside the crystal lattice [8,39].

(4) Limited practical capacity. The theoretical specific capacity of  $\text{V}_2\text{O}_5$  in Zn-ion systems is  $589 \text{ mAh}\cdot\text{g}^{-1}$  (for  $\text{V}^{5+}$  to  $\text{V}^{3+}$  transition). However, the specific capacity obtained in most published works is two to three times lower. Introducing CPs is a frequently adopted solution to increase the number of active sites and provide higher capacity. The composites of host material with CPs exhibit 20–200% higher specific capacity [8] and better cycling stability [40].

The progress in the development of AZIBs has been extensively reviewed, e.g., materials chemistry of AZIBs [40–43], energy storage mechanisms [29,44,45], microstructural engineering of cathode materials [46], layered vanadium oxides [47] and especially  $\text{V}_2\text{O}_5$ -based cathodes [48], etc. However, there are few reviews that emphasize the systematic investigation of CPs as components of composite vanadium-based cathodes in AZIBs,

while synthesis of composites is a promising strategy to improve functional properties by molecular pre-intercalation of CPs and by combining with nanostructuring and/or metal ion pre-intercalation. Therefore, a review on the optimization of cathode materials through the application of CPs, especially by pre-intercalation at the synthesis, and an uncovering of the relationship between structure and electrochemical and ion/electron transport properties is necessary. In this mini-review, we will summarize recent progress in the development of the vanadium-based composites with CPs as cathode materials for AZIBs, within the context of the effects that interlayer spacing, crystal structure, valence state, and morphology bear on the electrochemical response of the cathodes.

## 2. Conducting Polymer-Doped Vanadium Oxide-Based Cathodes for AZIBs

In general, the combination of nanosized active inorganic materials with CPs is recognized as a promising way of fabricating hybrid materials for battery electrodes, which combine unusual electrical, chemical, and mechanical properties. These approaches have been successfully proved in the case of lithium-ion batteries [49–51]. Similar approaches have been recently widely applied for vanadium-based cathodes for AZIBs.

Based on the  $\text{Zn}^{2+}$  insertion/extraction mechanism, cathode materials for AZIBs must possess a large interlayer spacing to accommodate hydrated  $\text{Zn}^{2+}$  ions. Most layered vanadium oxide-based compounds are composed of  $\text{VO}_x$  layers with weak van der Waals interactions, and the process of repeated intercalation/deintercalation of zinc ions can lead to irreversible phase transition and even structural collapse, limiting their performance [7, 41]. One of the most effective ways to solve these challenges is to pre-intercalate metal ions, water molecules or polymers as pillars into the cathode materials. Pre-intercalated species expand the interlayer spacing of the material and thus enhance its structural stability during the charge/discharge [40,52–54]. The pre-intercalation is also an efficient strategy to strengthen the layered structure of V-based oxides.

Water molecule intercalation is considered as an effective method for improving the long-term cycling performance of layered  $\text{V}_2\text{O}_5$  host structures because water molecules can expand the layer spacing of materials, decrease the strong electrostatic interaction between the V-O layer of the host framework and highly polarized  $\text{Zn}^{2+}$  ions [10], and provide flexibility in the host framework structure, accelerating the diffusion rate of  $\text{Zn}^{2+}$  ions [55]. Water molecules can also improve the reversibility of  $\text{Zn}^{2+}$  insertion/extraction, which results in high discharge specific capacity in cathode materials. Nevertheless, more studies are needed to identify the precise relationship between water molecule content and the electrochemical properties of materials [56]. When the water molecules are extracted from the interlayers of vanadium-based oxides, the corresponding electrochemical performance would degrade [10].

Preintercalated cations stabilize the layered structure due to the covalent linkage with host frameworks. However, excessively expanded interlayer spacing may cause unstable structures and possible structural collapse when subjected to repeated charge/discharge processes. Thus, it is necessary to maintain the balance of large interlayer spacing and structural stability in the host material. It was observed that intercalated CPs act as more robust structural pillars than cations and water molecules, enabling stable charging and discharging [57,58].

The intercalation of CPs into vanadium oxides and other vanadium-based compounds had attracted increasing attention due to their advantages for the improvement of the functional characteristics of electrode materials. The role of pre-intercalated CPs in improving the electrochemical performance of  $\text{V}_2\text{O}_5$  in AZIBs was confirmed by recent studies. On the one hand, the CPs, intercalated into layered vanadium oxide, can expand the interlayer spacing and stabilize the layered structures by lowering the Coulombic interactions between the guest  $\text{Zn}^{2+}$  and host framework, and can promote rapid diffusion of cations in the bulk phase [59], contributing to an enhanced capacity and long-term cycle stability [60]. On the other hand, the CP intercalated into vanadium oxide can partly reduce the oxidation state of vanadium, producing mixed valence states and thus enhancing its electronic

conductivity [61]. Unfortunately, the quantitative assessment of electronic conductivity is rarely given in works on vanadium oxide-based composites with CPs. The reported conductivity values for polyaniline-intercalated  $V_2O_5$  ranged from  $0.5$  to  $0.58 \text{ S}\cdot\text{cm}^{-1}$  [61,62] to  $0.01 \text{ S}\cdot\text{cm}^{-1}$  [63], the conductivity of polypyrrole-intercalated  $V_2O_5$  ranged from  $1.05$  to  $1.69 \times 10^{-4} \text{ S}\cdot\text{cm}^{-1}$  for composites with different polypyrrole content [64] and the electrical conductivities of PEDOT-modified  $V_2O_5$  were reported as  $1.17 \times 10^{-4} \text{ S}\cdot\text{cm}^{-1}$  [65] and  $9.28 \cdot 10^{-4} \text{ S}\cdot\text{cm}^{-1}$  [66].

$V_2O_5$  is also susceptible to dissolution in aqueous electrolytes during the charge–discharge cycling, which leads to capacity fading due to the loss of active material. The surface nanolayer coating of cathode materials with CPs is also an efficient material design strategy. The ultrathin protective CP layers provide structural integrity, effectively suppressing the cathode dissolution, alleviate volume changes during ions insertion/extraction, and, therefore, improve the cycling stability.

At present, polyaniline (PANI), polypyrrole (PPy), and poly(3,4-ethylenedioxythiophene) (PEDOT) are most commonly used for the preparation of vanadium oxide–CP composites (Figure 1). The advantages of CPs over other conductive materials (such as carbons or CNT additives) are in the better adhesion of the CP coating to the active material and tighter electrical contact between the electroactive particles, and the possibility of controlling their structure and properties by varying the conditions of the polymerization process.

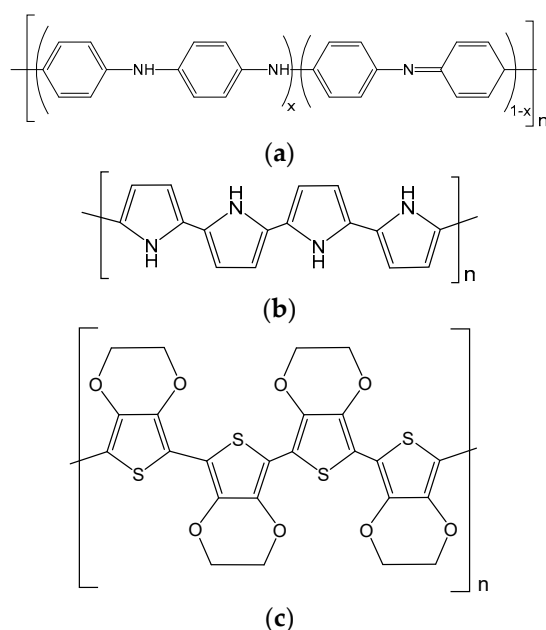


**Figure 1.** Structures of the most important conducting polymers. (a) Polyaniline; (b) Polypyrrole; (c) Poly-3,4-ethylenedioxythiophene.

CPs can be combined with the host materials via the controllable oxidation process by in situ polymerization of monomers [67–69], electrochemical polymerization [70], and interfacial polymerization [71]. Despite great advances in synthetic procedures, it is still a challenge to conduct precisely controlled syntheses to obtain materials with desired morphology and electrochemical performance.

The development of composites of vanadium-based materials with CPs for AZIBs started a few years ago, so the number of works published is not large, but the recent progress points at the future significance of composite cathode materials for AZIBs with CPs.

A wide range of conventional and state-of-the-art material characterization, surface analysis and electrochemical techniques have been applied to examine the performance and microstructural and chemical evolution of these novel cathode materials. The discussion will be mainly focused on the results obtained by electrochemical techniques used for battery evaluation (galvanostatic charge–discharge (GCD), electrochemical impedance spec-

troscopy (EIS), galvanostatic intermittent titration technique (GITT)), providing information on their capacitive and charge transfer processes.

### 2.1. Polyaniline-Modified Vanadium-Based Cathodes

Polyaniline (PANI), having a highly conjugated structure, high conductivity at low pH values [72,73], and light weight, has been widely used as a common conducting polymer in the field of energy storage, including AZIBs [74,75]. PANI can be introduced into layered vanadium-based materials by in situ or intercalative polymerization [53,60,62,63,67,76,77].

The lattice spacing of pristine  $V_2O_5$  powder is too small for direct intercalation of aniline molecules. To overcome this limitation, as a rule, water molecules are intercalated into  $V_2O_5$  before PANI intercalation. The resulting hydrated  $V_2O_5$  has expanded lattice spacing, which simplifies the subsequent intercalation of aniline monomers. Then, vanadium oxide–PANI composites can be synthesized via a facile intercalation–polymerization method. First, the hydrated  $V_2O_5$  is dispersed in the aniline monomer solution and anilinium cations are intercalated into the interlayer spaces of  $V_2O_5$ . In a second step, they undergo oxidative polymerization in the interlayer spaces of  $V_2O_5$ . During the PANI intercalation process, the valence of vanadium is partially reduced from +5 to +4 [59,61,78].

Polyaniline intercalation strategy was proposed for the first time in [53]. PANI-intercalated vanadium oxide (PVO) was obtained by one-step in situ oxidative polymerization with intercalation of aniline into vanadium oxide according to an earlier procedure (Figure 2a) [59]. During the oxidative polymerization of aniline,  $V^{5+}$  was partially reduced to  $V^{4+}$  while polyaniline was formed between the layers of vanadium oxide. According to TGA analysis, the content of PANI in the PVO composite was 10.8 wt. %. According to the XPS data, the atomic ratios of  $V^{4+}$  and  $V^{5+}$  were 31.68% and 68.32%, respectively. After polyaniline and water co-intercalation, the interlayer spacing was expanded from 5.77 Å of  $V_2O_5$  to 14.02 Å in PVO, facilitating the ion diffusion. The partial reduction of  $V^{5+}$  to  $V^{4+}$  in the lattice and  $\pi$ -conjugated network of PANI enhanced the charge transport properties of the PVO. The AZIB utilizing the obtained PVO cathode delivered high specific discharge capacity (420.4 mAh·g<sup>-1</sup> at 0.5 A·g<sup>-1</sup>), a prominent rate capability (400 mAh·g<sup>-1</sup> at 5 A·g<sup>-1</sup> and 288.9 mAh·g<sup>-1</sup> at 20.0 A·g<sup>-1</sup>) and high capacity retention (87.5% after 600 cycles at 5 A·g<sup>-1</sup>), although the gradual increase of the specific capacity during about 20 cycles points at the slow activation of the cathode material. A combined intercalation and conversion reaction mechanism of  $Zn^{2+}$  ion storage in the PVO was confirmed by ex situ XRD and ex situ high-resolution XPS spectroscopy. During the discharge process, an electrochemically active intermediate phase ( $Zn_3(OH)_2(V_2O_7) \cdot 2H_2O$ ) was formed upon  $Zn^{2+}$  intercalation into PVO, and upon further discharging this phase evolved into  $Zn_x(PVO)_y$ . At the fully charged state  $Zn_x(PVO)_y$  and  $Zn_3(OH)_2(V_2O_7) \cdot 2H_2O$  coexisted (Figure 2b).

Another organic–inorganic hybrid material was prepared in [67]. Refabricated  $V_2O_5$  ( $r\text{-}V_2O_5$ ) was integrated with PANI by chemical oxidation polymerization to synthesize a  $V_2O_5@PANI$  nanocomposite with 17 wt. % of PANI in it. The organic–inorganic  $V_2O_5@PANI$  nanocomposite displayed a uniform three-dimensional porous morphology with PANI layer on the surface of the composite particles. The V 2p peaks on the XPS spectra of  $V_2O_5@PANI$  shifted to lower binding energies compared with those of initial  $r\text{-}V_2O_5$ , suggesting the existence of  $V^{4+}$  due to a partial reduction of  $V^{5+}$  to  $V^{4+}$ . The  $V_2O_5@PANI$  nanocomposite electrode delivered a high reversible capacity of 361 mAh·g<sup>-1</sup> at the current density of 0.1 A·g<sup>-1</sup>, a high-rate capability (201 mAh·g<sup>-1</sup> at 5 A·g<sup>-1</sup>) that was much better than that of unmodified  $r\text{-}V_2O_5$  and PANI.  $V_2O_5@PANI$  exhibited better long-term cyclability and delivered a higher and more stable discharge capacity (201 mAh·g<sup>-1</sup>) than  $r\text{-}V_2O_5$  (147 mAh·g<sup>-1</sup>) and PANI (52 mAh·g<sup>-1</sup>) at 5 A·g<sup>-1</sup> up to 1000 cycles.  $V_2O_5@PANI$  exhibited high power density (5958 W·kg<sup>-1</sup>) and high energy density (252 Wh·kg<sup>-1</sup>) calculated based on the mass of the cathode material. The EIS study had shown that the charge-transfer resistance of  $V_2O_5@PANI$  is much lower (126 Ohm) than that of  $r\text{-}V_2O_5$  (158 Ohm). The diffusion coefficient of  $Zn^{2+}$  in the  $V_2O_5@PANI$  and  $r\text{-}V_2O_5$  cathodes was determined by the GITT. The  $V_2O_5@PANI$  nanocomposite demonstrated faster diffusion kinetics, and the  $Zn^{2+}$  diffusion coefficient value for  $V_2O_5@PANI$  electrode

during the discharging process was estimated to be  $1.3 \times 10^{-7}$ – $1.1 \times 10^{-9} \text{ cm}^2 \text{ s}^{-1}$ , higher than  $1.2 \times 10^{-8}$ – $1.9 \times 10^{-10} \text{ cm}^2 \text{ s}^{-1}$  for  $r\text{-V}_2\text{O}_5$  electrode.

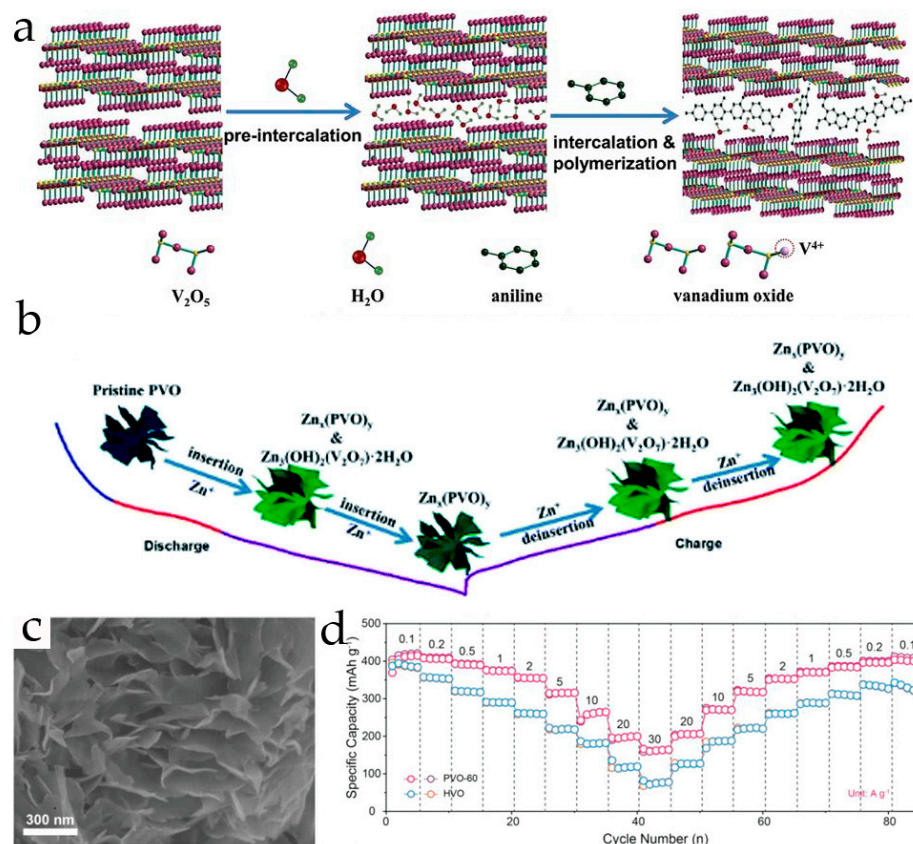


**Figure 2.** (a) Scheme of the PVO preparation processes [53]; (b) Scheme of the reversible zinc storage mechanism in the PVO electrode [53]; (c) SEM image of as-prepared PVO-60 sample [60]; (d) Rate capability of PVO-60 and HVO at various current densities [60].

An in situ polymerization reaction was also adopted to prepare PANI-intercalated  $\text{V}_2\text{O}_5$  nanosheets (PVO) (Figure 2c) with an interlayer distance of  $13.90 \text{ \AA}$  [60]. Samples with different component ratios were prepared. During the repetitive  $\text{Zn}^{2+}$  intercalation and deintercalation, the PVO exhibited a stable and highly reversible electrochemical response. It was shown by in situ synchrotron XRD that the  $\pi$ -conjugated network of PANI effectively decreases electrostatic interactions between the  $\text{Zn}^{2+}$  and  $\text{O}^{2-}$  of the host lattice, thus facilitating the  $\text{Zn}^{2+}$  diffusion. The DFT calculations had shown that the interlayer PANI caused a move of the Fermi level toward the conduction band, as a result, facilitating the electron transfer. It was also shown that the  $\pi$ -conjugated network of PANI leads to a remarkable decrease in the binding energy between  $\text{Zn}^{2+}$  and host  $\text{O}^{2-}$  in the V–O layer in PVO (1.67 eV) compared with that of pristine  $\text{V}_2\text{O}_5$  (2.06 eV), which explains the enhanced diffusion kinetics of  $\text{Zn}^{2+}$  in PANI-intercalated  $\text{V}_2\text{O}_5$ . As a result, PVO showed high-rate capability (Figure 2d) and excellent rate performance ( $197.1 \text{ mAh} \cdot \text{g}^{-1}$  at  $20 \text{ A} \cdot \text{g}^{-1}$ ) and an outstanding long-term cycling stability (97.6% capacity retention after 2000 cycles).

A similar in situ intercalation procedure was used to obtain PANI-intercalated  $\text{V}_2\text{O}_5$  hybrid electrode materials in [76]. The structure of resulting PANI-intercalated vanadium oxide (PIVO) was also tuned by selecting the  $\text{V}_2\text{O}_5$ -to-aniline ratio and adjusting the temperature, so that the reversible accommodation of  $\text{Zn}^{2+}$  was achieved in the resultant PIVO with enlarged layer spacing. According to the ICP-MS results, the PIVO composite with the molecular formula  $\text{V}_2\text{O}_5 \cdot 0.3\text{C}_6\text{H}_6\text{N} \cdot 1.5\text{H}_2\text{O}$  was formed. The PIVO electrode exhibited a large specific capacity of  $372 \text{ mAh} \cdot \text{g}^{-1}$  at  $0.5 \text{ A} \cdot \text{g}^{-1}$ , and PANI as a pillar also endowed good cycling stability of the composite. In situ XRD and IR studies had

shown that intercalated PANI species not only enlarge the interlayer spacing for  $\text{Zn}^{2+}$  storage, but PIVO structure also allows the accumulation of additional zinc ions without phase transformation. Conjugated polymeric chains improve the stability by buffering the structural expansion due to polymer structure flexibility. Pre-intercalated PANI molecules enable the reversible intercalation of  $\text{Zn}^{2+}$  and/or  $\text{H}^+$  ions in layered  $\text{V}_2\text{O}_5$ , leading to improved battery performance via the synergistic effect.

In [54], a PANI-intercalated hydrated  $\text{V}_2\text{O}_5$  composite (PANI/ $\text{V}_2\text{O}_5$ ) was obtained through a mild molecule-exchange reaction at room temperature. First, the hydrated  $\text{V}_2\text{O}_5$  hydrogel was fabricated using a hydrothermal method at  $120\text{ }^\circ\text{C}$  for 6 h, and then the PANI/ $\text{V}_2\text{O}_5$  composite was synthesized by vigorously stirring the prepared hydrated  $\text{V}_2\text{O}_5$  hydrogel with an aqueous solution of aniline monomer for 6 h at room temperature.

The redox reaction in PANI/ $\text{V}_2\text{O}_5$  composite [54] was studied by cyclic voltammetry. The CV curves revealed a highly reversible  $\text{Zn}^{2+}$  intercalation/deintercalation redox reaction, although the first several CVs showed a small difference in shape, which can be attributed to the gradual activation process of the freshly prepared electrode. Two pairs of peaks at 0.6 V and 1.0 V, originating from the  $\text{V}^{4+}/\text{V}^{3+}$  and  $\text{V}^{5+}/\text{V}^{4+}$  transitions, respectively, were observed (Figure 3a). The reaction kinetics of the  $\text{Zn}^{2+}$  ions solid-state diffusion in the PANI/ $\text{V}_2\text{O}_5$  composite were studied by GITT (Figure 3b). The diffusion coefficient of  $\text{Zn}^{2+}$  ions was found as high as  $10^{-9}$ – $10^{-10}\text{ cm}^2\cdot\text{s}^{-1}$  (Figure 3c) and can account for the relatively spacious open inner space and the tunnel structure of the composite. The PANI/ $\text{V}_2\text{O}_5$  composite electrode demonstrated stable and highly specific capacities at current densities from 0.1 to  $4\text{ A}\cdot\text{g}^{-1}$ . The reversible specific capacity of PANI/ $\text{V}_2\text{O}_5$  was  $353.6\text{ mAh}\cdot\text{g}^{-1}$  at  $0.1\text{ A}\cdot\text{g}^{-1}$ , and  $278.3\text{ mAh}\cdot\text{g}^{-1}$  at  $4\text{ A}\cdot\text{g}^{-1}$ . After continuous charging/discharging for 100 cycles at  $0.2\text{ A}\cdot\text{g}^{-1}$ , 87.5% capacity retention with a 100% coulombic efficiency was observed. The maximum energy and power density of PANI/ $\text{V}_2\text{O}_5$  were  $258\text{ Wh}\cdot\text{kg}^{-1}$  and  $2784\text{ W}\cdot\text{kg}^{-1}$ , respectively.

A quite similar synthesis procedure was used to obtain PANI-intercalated  $\text{V}_2\text{O}_5$  (PAVO) hybrids in [63]. The PAVO cathode for AZIBs, which operated for about 1 month, delivered a specific capacity of  $350\text{ mAh}\cdot\text{g}^{-1}$  with a capacity retention of  $\sim 90\%$  (over 100 cycles at  $0.1\text{ A}\cdot\text{g}^{-1}$ ). The experimental studies were supported by first-principle DFT calculations to evaluate the binding energies and intercalation behavior of  $\text{Zn}^{2+}$  ion in the two-layered structures of pristine hydrated vanadium oxide (VHO) and polyaniline-intercalated vanadium oxide (PAVO) (Figure 3d,e). The binding energies were calculated by replacing water molecule with aniline molecule in the interlayer space, and a significantly lower binding energy of  $-124.5\text{ kJ}\cdot\text{mol}^{-1}$  by intercalating organic molecule compared with  $\text{H}_2\text{O}$  ( $-21.3\text{ kJ}\cdot\text{mol}^{-1}$ ) was found (Figure 3f). Therefore, it was shown that the removal of water from the interlamellar space followed by the insertion of a monolayer of polyaniline is a spontaneous process. As aniline molecules polymerize together with the intercalation process, most water molecules will be replaced by polyaniline. The calculation also confirmed a weak hydrogen bond, which stabilizes and preserves the layered  $\text{V}_2\text{O}_5$  matrix when cycling.

Another vanadium oxide ( $\text{V}_2\text{O}_{5-x}$ )/PANI composite (PANI-V) was synthesized by the intercalation–polymerization method from  $\text{V}_2\text{O}_5\cdot n\text{H}_2\text{O}$  xerogel and aniline solution in methanol in [79]. The PANI-V superlattice structure retained the nanosheet-like morphology of  $\text{V}_2\text{O}_5$ , and the interlayer spacing was expanded to  $15.6\text{ \AA}$ . The results of HR-TEM, Raman spectroscopy, XPS, and FTIR confirmed that PANI intercalated into the  $\text{V}_2\text{O}_5$ . The electrochemical performance of PANI-V composite was evaluated in the coin cells vs. Zn anode in  $2\text{ M ZnSO}_4$  aqueous electrolyte. Notably, the PANI-V electrode did not undergo an activation process during cycling. At the current density of  $100\text{ mA}\cdot\text{g}^{-1}$ , the PANI-V electrode demonstrated the highest capacity of  $490\text{ mAh}\cdot\text{g}^{-1}$ , compared to  $275\text{ mAh}\cdot\text{g}^{-1}$  of  $\text{V}_2\text{O}_5\cdot n\text{H}_2\text{O}$  xerogel and  $152\text{ mAh}\cdot\text{g}^{-1}$  of commercial  $\text{V}_2\text{O}_5$ , due to the expanded interlayer spacing of PANI-V and the improved electrical conductivity of the material. This was also verified by rate capability tests. PANI-V electrode presented excellent high-rate capability, and the capacity of 283, 265, 254, 249, and  $234\text{ mAh}\cdot\text{g}^{-1}$  at the rates of 2, 5, 10, 16, and 32 C ( $1\text{ C} = 500\text{ mA}\cdot\text{g}^{-1}$ ), respectively, while the capacity of  $\text{V}_2\text{O}_5\cdot n\text{H}_2\text{O}$  dropped dramatically

at high rates. The diffusion coefficients ( $D$ ) of  $Zn^{2+}$  for PANI-V and  $V_2O_5 \cdot nH_2O$  during the discharge–charge process determined by GITT demonstrate that the diffusion kinetics of  $Zn^{2+}$  through the  $V_2O_5$  layers were greatly improved by PANI intercalation into the structure. The  $D$  values of PANI-V were within the range of  $0.4 \times 10^{-8}$ – $5.2 \times 10^{-8} \text{ cm}^2 \cdot \text{s}^{-1}$ , compared to  $0.1 \times 10^{-9}$ – $2.4 \times 10^{-9} \text{ cm}^2 \cdot \text{s}^{-1}$  of  $V_2O_5 \cdot nH_2O$ .

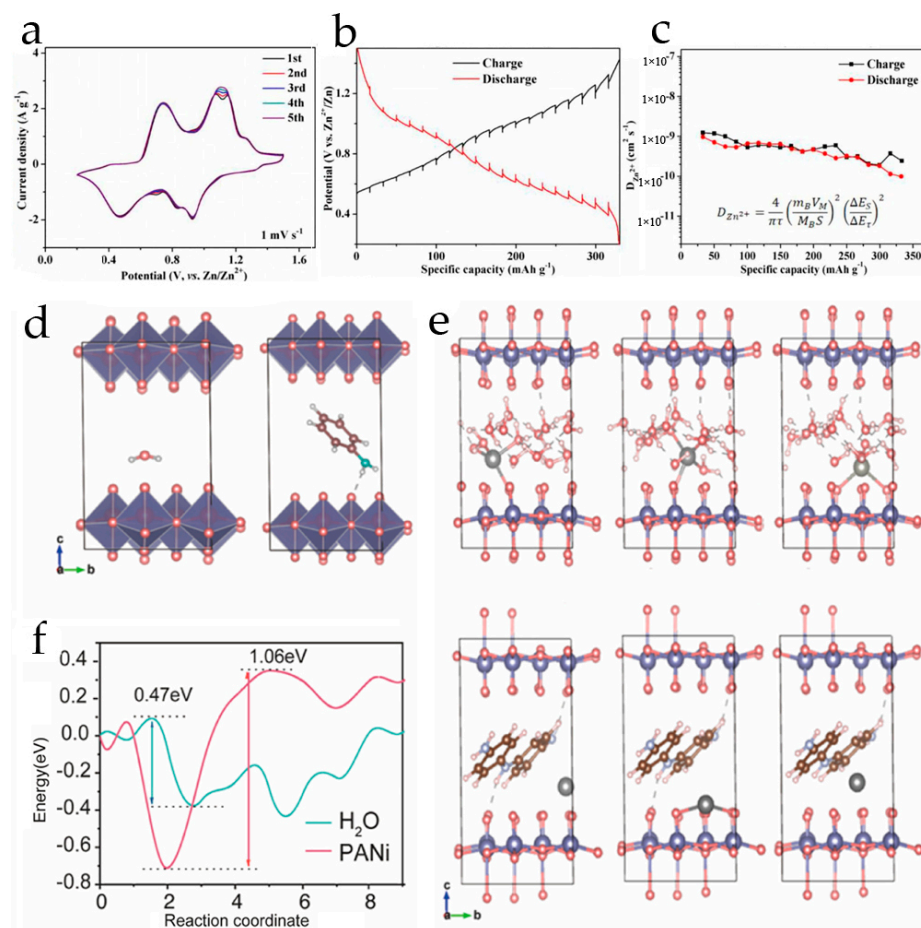


**Figure 3.** (a) CV curves of PANI/ $V_2O_5$  composite in the first five cycles at  $1 \text{ mV} \cdot \text{s}^{-1}$  [54]; (b) The GITT curves and (c) the calculated diffusion coefficient of  $Zn^{2+}$  of PANI/ $V_2O_5$  composite [54]; (d) Models for calculating binding energies of water- and aniline-intercalated  $V_2O_5$  matrix [63]; (e) possible Zn ion migration pathway in VHO and PAVO. Blue, red, and grey balls represent V, O, and Zn atoms, respectively [63]; (f) energy barriers along Zn migration pathways for VHO and PAVO [63].

Similarly, polyaniline-intercalated hydrated vanadium pentoxide (PANI-VOH) hybrid composite was synthesized by an interface–intercalation method from the vanadium oxide (VOH) hydrogel dispersion in water and aniline solution in  $CCl_4$  [77]. When the two phases came into contact, the aniline monomers diffused to the  $CCl_4$ /water interface and intercalated in situ into the interlayer space of VOH. During the intercalation process, water molecules in the interlayer space of the VOH hydrogel were partially replaced by the aniline monomers, which polymerized due to the oxidative effect of VOH and dissolved oxygen. The in situ oxidative polymerization/intercalation of aniline was completed in air. The PANI-VOH had a 3D sponge-like architecture of nanosheets with a corrugated surface and  $14.1 \text{ \AA}$  interlayer spacing. The FTIR and Raman spectra of the PANI-VOH proved that PANI was successfully intercalated into vanadium oxide hydrogel as a pillar to form the composite. According to TGA, the content of PANI in PANI-VOH was about 12.8 wt. %. The specific capacities of PANI-VOH were much higher than of pristine VOH at every current density, and the composite demonstrated stable cycling performance. The initial discharge capacity of PANI-VOH and VOH cathodes at  $0.1 \text{ A} \cdot \text{g}^{-1}$  was 343

and  $225 \text{ mAh}\cdot\text{g}^{-1}$ , respectively. The ex situ XRD and XPS had shown that during the first intercalation/deintercalation of  $\text{Zn}^{2+}$ , a minor part of PANI-VOH was converted into  $\text{Zn}_3(\text{OH})_2\text{V}_2\text{O}_7\cdot 2\text{H}_2\text{O}$ . Then, the PANI-VOH and  $\text{Zn}_3(\text{OH})_2\text{V}_2\text{O}_7\cdot 2\text{H}_2\text{O}$  co-existed, and the stability of CV and GCD curved during charge/discharge points at the reversibility of the process. The distinct Zn 2p peaks on the ex situ XPS spectra of the PANI-VOH cathode at the fully discharged state confirmed the intercalation of  $\text{Zn}^{2+}$  into the PANI-VOH. At the fully charged state, weak Zn 2p peaks were also observed due to the abovementioned irreversible partial phase transformation of PANI-VOH to  $\text{Zn}_3(\text{OH})_2\text{V}_2\text{O}_7\cdot 2\text{H}_2\text{O}$ .

In [62], the PANI-vanadium oxide (PVO) hybrid material with a  $14.1 \text{ \AA}$  interlayer spacing was synthesized by the hydrothermal method at  $150 \text{ }^\circ\text{C}$ . During the synthesis, PANI was doped with p-toluenesulfonic acid to improve its conductivity. According to the TGA, PANI content in PVO was 7.8 wt. %. The PVO electrode demonstrated a high reversible capacity of  $356 \text{ mAh}\cdot\text{g}^{-1}$  at  $0.1 \text{ A}\cdot\text{g}^{-1}$  and maintained a high capacity ( $235 \text{ mAh}\cdot\text{g}^{-1}$ ) even at a high current density of  $20 \text{ A}\cdot\text{g}^{-1}$  and excellent rate capability. The rate performance and cycling stability of the PVO cathode were improved due to the high electronic conductivity of PVO ( $0.58 \text{ S}\cdot\text{cm}^{-1}$ ), fast  $\text{Zn}^{2+}$  migration rate and enhanced interlayer structure due to intercalated polyaniline. PVO maintained high capacity retention (96.3%) and almost 100% Coulombic efficiency after 1000 cycles at  $5 \text{ A}\cdot\text{g}^{-1}$ , demonstrating its outstanding cycling stability. The PVO electrode had shown no obvious change in morphology and composition after long-term cycling, demonstrating its good structural stability.

Polyaniline-intercalated and exfoliated hydrated vanadium oxide ( $\text{V}_2\text{O}_5\cdot n\text{H}_2\text{O}$ , VOH) cathode material (PANI-VOH) was prepared in [80]. Freshly synthesized VOH in solution was mixed with acidic (pH 2) aqueous aniline solution, and the mixture was kept at  $120 \text{ }^\circ\text{C}$  for 3 h. The low-temperature oxidation process resulted in the formation of PANI structures with long chains, which promoted the exfoliation of VOH. The content of PANI in the PANI-VOH composite calculated from TGA was about 11%. According to the BET tests results, the surface area of PANI-VOH was  $62.45 \text{ m}^2\cdot\text{g}^{-1}$ , much higher than that of VOH ( $2.53 \text{ m}^2\cdot\text{g}^{-1}$ ). The wide pore size distribution of PANI-VOH (4–100 nm) was attributed to the stacking of the exfoliated sheets. The PANI-VOH electrode in the “water-in-salt”  $3 \text{ M Zn}(\text{CF}_3\text{SO}_3)_2 + 6 \text{ M LiTFSI}$  electrolyte demonstrated the specific capacity of  $323 \text{ mAh}\cdot\text{g}^{-1}$  at  $1 \text{ A}\cdot\text{g}^{-1}$ , and good cycling stability with 80% capacity retention after 800 cycles. Due to facile redox kinetics of the material, the PANI-VOH AZIB possessed the specific energy of  $216 \text{ Wh}\cdot\text{kg}^{-1}$  at  $252 \text{ W}\cdot\text{kg}^{-1}$ , and  $150 \text{ Wh}\cdot\text{kg}^{-1}$  at  $3900 \text{ W}\cdot\text{kg}^{-1}$ . EIS and GITT analyses indicated that, compared to VOH, PANI-VOH demonstrated a significant decrease in the charge transfer resistance and higher  $\text{Zn}^{2+}$  diffusivity during charge and discharge. Fast kinetics of charge–discharge allowed the  $\text{V}^{5+}/\text{V}^{3+}$  redox transition of material, while intercalated PANI facilitated the electrical conductivity of the electrode and maintained structural stability of the composite during cycling.

The incorporation of PANI molecules into the interlayers of  $\text{V}_2\text{O}_5$  significantly expands the interlayer spacing of vanadium oxide, stabilizes the layered structure, and promotes facile  $\text{Zn}^{2+}$  diffusion. The  $\text{V}_2\text{O}_5$ -PANI nanocomposites as cathode materials possess faster electron transfer and ion diffusion than unmodified  $\text{V}_2\text{O}_5$ , thus realizing excellent long-term cycle performance and rate capability. Simple yet effective strategies for the incorporation of PANI allowed advanced cathode materials to develop with emerging storage properties for AZIBs.

## 2.2. Polypyrrole-Modified Vanadium-Based Cathodes

Polypyrrole (PPy) is a popular conducting polymer for battery applications due to its high conductivity, low toxicity, and facile synthesis [81]. PPy can be prepared via the oxidative polymerization of pyrrole and has higher stability and conductivity than PANI [82]. The yield, morphology, and electrical conductivity of PPy are determined by the nature of the oxidant and the reaction conditions [83]. The electrode reaction of the PPy involves both electron and ion transport within the film [84].

$V_2O_5$  nanowires were wrapped into polypyrrole in [81] to obtain a  $V_2O_5$ /PPy composite by a surface-initiated polymerization of pyrrole at room temperature. Pyrrole was dissolved in DMF and slowly added to  $V_2O_5$  nanowires dispersed in water. The solution was vigorously stirred for 24 h for polymerization.  $V_2O_5$  as an oxidant induced the polymerization of pyrrole on its surface. No significant changes were observed on the XRD of  $V_2O_5$  after coating by PPy, indicating that the layered oxide structure with 9.6 Å spacing was well maintained after the polymerization. The XPS spectra demonstrated the presence of a 9.3 at. % of  $V^{4+}$ , corresponding to the generation of oxygen vacancies on the  $V_2O_5$  surface. The PPy-coated  $V_2O_5$  nanowires had higher electronic conductivity; as a protective layer PPy also decreased the  $V_2O_5$  dissolution. The  $V_2O_5$ /PPy cathode delivered a high initial capacity of  $466 \text{ mAh}\cdot\text{g}^{-1}$  at  $0.1 \text{ A}\cdot\text{g}^{-1}$ , while the initial  $V_2O_5$  nanowires delivered  $425 \text{ mAh}\cdot\text{g}^{-1}$ .  $V_2O_5$ /PPy demonstrated better rate performance than unmodified  $V_2O_5$  in the entire range of studied current densities (up to of  $5.0 \text{ A}\cdot\text{g}^{-1}$ ). The kinetics of the  $V_2O_5$ /PPy composite cathode was studied by GITT. The  $Zn^{2+}$  diffusion coefficient for  $V_2O_5$ /PPy during discharging–charging procedures was  $3.03 \times 10^{-9}$ – $1.46 \times 10^{-10} \text{ cm}^2\cdot\text{s}^{-1}$ .

The composite of hydrated vanadium oxide with polypyrrole (PPy/VOH) was synthesized (Figure 4a) at room temperature by dripping pyrrole monomer into hydrated vanadium oxide under continuous stirring in [85]. The pyrrole monomers, intercalated into the VOH layers, were oxidized by vanadium oxide and polymerized into chain-like polypyrrole, which extended the V–O layers spacing. The insertion of pyrrole was confirmed by powder XRD data (Figure 4b). The intercalation of PPy resulted in the decrease in crystallinity of PPy/VOH and the intensity of X-ray diffraction peaks. As can be seen from the high-resolution TEM image (Figure 4c), the interlayer spacing of vanadium oxide was expanded to 14.0 Å. The percentage of PPy in PPy/VOH determined by the TGA was 12.48 wt. %. The galvanostatic charge–discharge tests have shown that the specific capacity of PPy/VOH is much larger than that of VOH. Rate capability tests of both materials have shown that the discharge capacities of PPy/VOH were 383, 351, 327, 303 and 281  $\text{mAh}\cdot\text{g}^{-1}$  at the current densities of 0.1, 0.2, 0.5, 1 and  $2 \text{ A}\cdot\text{g}^{-1}$ , respectively, compared to  $48 \text{ mAh}\cdot\text{g}^{-1}$  at  $2 \text{ A}\cdot\text{g}^{-1}$  of VOH (Figure 4d). The specific capacity of PPy was  $56 \text{ mAh}\cdot\text{g}^{-1}$  at  $0.2 \text{ A}\cdot\text{g}^{-1}$  and decreased during cycling, so it makes a small contribution to the PPy/VOH capacity. The cyclic stability of the composite material was not perfect, which was explained by the low cyclic stability of PPy due to repeated swelling/contraction of the polymer. The diffusion coefficient of  $Zn^{2+}$  in the PPy/VOH cathode calculated from GITT conducted at  $0.5 \text{ A}\cdot\text{g}^{-1}$  was  $10^{-8}$ – $10^{-9} \text{ cm}^2\cdot\text{s}^{-1}$ , while in VOH it was only about  $10^{-10} \text{ cm}^2\cdot\text{s}^{-1}$ . The obtained  $Zn^{2+}$  diffusion coefficients in PPy/VOH were higher than in some other PANI-intercalated vanadium oxide composites [60,80], and were attributed to the expanded interlayer spacing due to insertion of PPy, which facilitated the transport of zinc ions. The energy density of the PPy/VOH-based AZIB was  $358 \text{ Wh}\cdot\text{kg}^{-1}$  at the power density of  $95 \text{ W}\cdot\text{kg}^{-1}$ , and  $303 \text{ Wh}\cdot\text{kg}^{-1}$  at  $2164 \text{ W}\cdot\text{kg}^{-1}$ , which is superior to some other reported polymer-intercalated VOH cathode materials, for example, PANI/ $V_2O_5$  ( $258.3 \text{ Wh}\cdot\text{kg}^{-1}$ ) [54], PANI-VOH ( $225 \text{ Wh}\cdot\text{kg}^{-1}$ ) [80] and  $V_2O_5$ @PEDOT ( $280 \text{ Wh}\cdot\text{kg}^{-1}$ ) [57].

The polypyrrole-intercalated  $V_2O_5$  (PPy-V) was obtained through a hydrothermal reaction at  $120 \text{ }^\circ\text{C}$  [86]. Samples with different PPy content have been obtained. According to TGA, the weight content of PPy in PPy-V-10 was 4.1%. The diffraction patterns of PPy-intercalated  $V_2O_5$  were completely different from orthogonal  $V_2O_5$  (Figure 4e). The as-prepared PPy-V-10 sample exhibited a “foliated rock” architecture consisting of numerous nanoflakes. The two plateaus clearly observed in the charge/discharge profiles of PPy-V-10 (Figure 4f) were in agreement with the CV test results. During long-term cycling at low current densities ( $0.2 \text{ A}\cdot\text{g}^{-1}$ ), the gradual increase of charge–discharge capacity was initially observed due to the activation process (Figure 4g). Then the capacity decreased slowly, probably due to continuous damage of the structure caused by the deep charge–discharge processes. The PPy-V electrode exhibited excellent rate capability and high reversible discharge capacities at high current densities ( $290$  and  $241 \text{ mAh}\cdot\text{g}^{-1}$  at  $2$  and  $5 \text{ A}\cdot\text{g}^{-1}$ , respectively). The battery had shown a high energy density of  $362 \text{ Wh}\cdot\text{kg}^{-1}$  at a power density of  $200 \text{ W}\cdot\text{kg}^{-1}$ , and even at ultra-high densities of  $5000 \text{ W}\cdot\text{kg}^{-1}$  the energy

density of  $240 \text{ Wh}\cdot\text{kg}^{-1}$  was maintained. This is superior to some other vanadium-based composites with CPs for AZIBs, PEDOT-NVO [87] and PANI-VOH [80]. By means of GITT, EIS and ex situ XRD it was shown that the energy storage mechanism of the PPy-V was a stepwise  $\text{H}^+/\text{Zn}^{2+}$  co-intercalation.

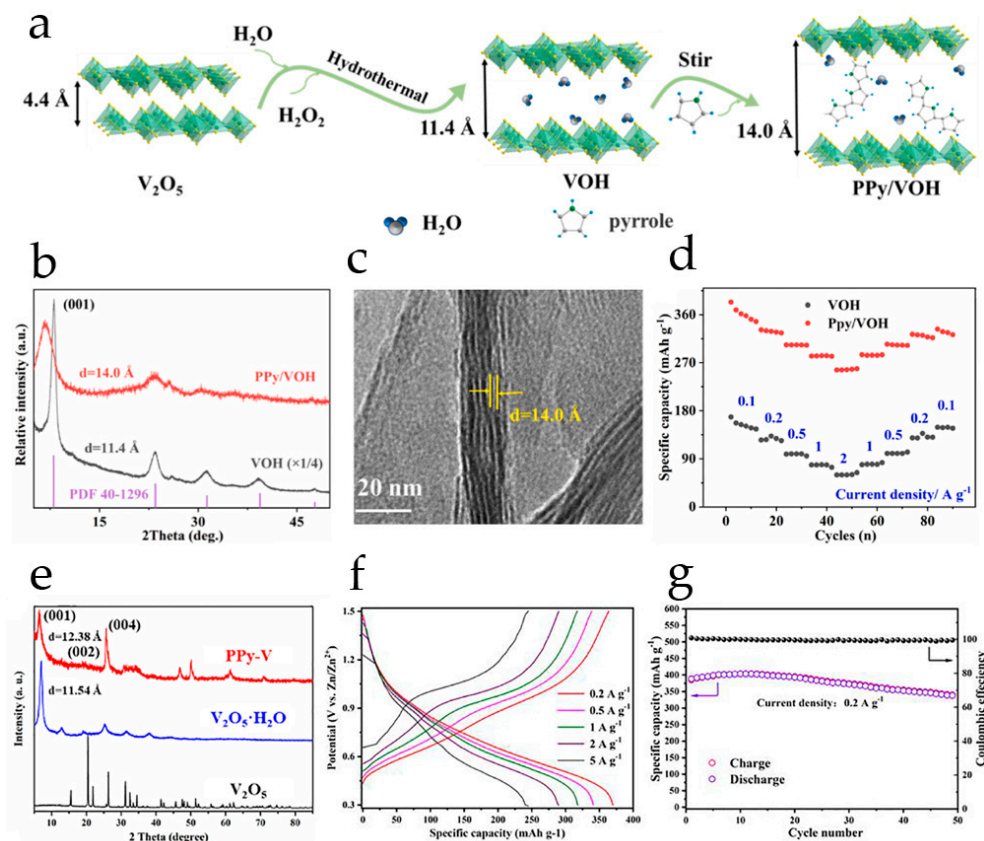


**Figure 4.** (a) Scheme of the PPy/VOH composite synthesis [85]; (b) XRD patterns of VOH and PPy/VOH [85]; (c) HRTEM image of PPy/VOH [85]; (d) Rate capability of VOH and PPy/VOH at current densities  $0.1\text{--}2 \text{ A}\cdot\text{g}^{-1}$  [85]; (e) XRD patterns of PPy-V,  $\text{V}_2\text{O}_5\cdot\text{H}_2\text{O}$  and  $\text{V}_2\text{O}_5$  for comparison [86]; (f) Charge–discharge curves of PPy-V-10 electrode at current densities  $0.2\text{--}5 \text{ A}\cdot\text{g}^{-1}$  [86]; (g) Cycling performance of PPy-V-10 electrode (50 cycles at  $0.2 \text{ A}\cdot\text{g}^{-1}$ ) [86].

Among the various modification strategies, oxygen defect engineering is particularly attractive as it can modify electronic structures without significant alteration to the lattice, which could lead to the improvement of the electrochemical performance. Oxygen vacancies help to facilitate the charge transfer kinetics due to a larger interlayer spacing in the material, which allows the retention of the structural integrity during cycling [88].

$\text{V}_2\text{O}_5$ -polypyrrole nanobelt composites were obtained by in situ polymerization at room temperature in [64]. In the course of the polymerization,  $\text{V}_2\text{O}_5$  served as an oxidant, and pyrrole polymerized on the surface of  $\text{V}_2\text{O}_5$  to form the  $\text{V}_2\text{O}_5$ -PPy core-shell nanoparticles. Depending on the component ratio, the content of PPy in  $\text{V}_2\text{O}_5$ -PPy samples ranged 7–15 wt. %. With the increase of PPy content in the composite, the atomic percentage of  $\text{V}^{5+}$  in the  $\text{V}_2\text{O}_5$ -PPy, calculated from the corresponding peak areas of the XPS spectra, gradually decreased, and that of  $\text{V}^{4+}$  increased, indicating that the concentration of oxygen vacancies gradually increased [89]. The sample with 9 wt. % PPy content,  $\text{V}_2\text{O}_5$ -9PPy, had shown formidable specific capacities (e.g.,  $441 \text{ mAh}\cdot\text{g}^{-1}$  at  $0.1 \text{ A}\cdot\text{g}^{-1}$  and  $291 \text{ mAh}\cdot\text{g}^{-1}$  at  $5.0 \text{ A}\cdot\text{g}^{-1}$ ) and excellent rate performance. When returning to  $0.1 \text{ A}\cdot\text{g}^{-1}$ ,  $\text{V}_2\text{O}_5$ -9PPy maintained a specific capacity of  $441 \text{ mAh}\cdot\text{g}^{-1}$ .  $\text{V}_2\text{O}_5$ -9PPy also showed high energy densities:  $284 \text{ Wh}\cdot\text{kg}^{-1}$  at  $70 \text{ W}\cdot\text{kg}^{-1}$  power density, and  $2586 \text{ W}\cdot\text{kg}^{-1}$  at  $173 \text{ Wh}\cdot\text{kg}^{-1}$ . According to the EIS data, the  $\text{V}_2\text{O}_5$ -9PPy sample also exhibited the lowest charge transfer

resistance, indicating the fastest kinetics, which also explained its excellent rate performance. The zinc ion diffusion coefficient ( $4.4 \times 10^{-8}$ – $1.62 \times 10^{-9}$   $\text{cm}^2 \text{s}^{-1}$ ), indicating good kinetics, was evaluated by GITT at  $0.1 \text{ A}\cdot\text{g}^{-1}$ . The electronic conductivity of  $\text{V}_2\text{O}_5$ -based electrodes and composites with different amounts of PPy was measured by four-point probe technique. As the amount of PPy increased, the electronic conductivity of  $\text{V}_2\text{O}_5$ -PPy was improved. The conductivity of  $\text{V}_2\text{O}_5$  was  $4.9 \times 10^{-6}$   $\text{S}\cdot\text{cm}^{-1}$ , and  $1.05 \times 10^{-4}$ ,  $1.36 \times 10^{-4}$  and  $1.69 \times 10^{-4}$   $\text{S}\cdot\text{cm}^{-1}$  for composites with 7, 9 and 15 wt. % of polypyrrole, respectively [64].

A composite cathode of  $\text{V}_2\text{O}_5$  coated by a layer of PPy ( $\text{V}_2\text{O}_5$ @PPy) was synthesized in [39], in an ice-bath under a nitrogen atmosphere using  $\text{FeCl}_3$  as an oxidizing agent. The morphology of  $\text{V}_2\text{O}_5$ @PPy sample was grained, similar to that of pristine  $\text{V}_2\text{O}_5$ , suggesting a thin-layer coating of PPy. A layer of PPy film uniformly deposited on  $\text{V}_2\text{O}_5$  particles could be seen clearly on the TEM image. All the characteristic peaks of  $\text{V}_2\text{O}_5$  were observed in the XRD spectrum of  $\text{V}_2\text{O}_5$ @PPy composite, demonstrating that the PPy coating does not affect the crystal structure of  $\text{V}_2\text{O}_5$ . The  $\text{V}_2\text{O}_5$ @PPy cathode presented a moderate initial discharge capacity of  $109.6 \text{ mAh}\cdot\text{g}^{-1}$  at  $1 \text{ A}\cdot\text{g}^{-1}$  and maintained a 95.6% capacity retention after 300 cycles. The discharge capacity increased gradually during ca. 100 cycles up to nearly  $150 \text{ mAh}\cdot\text{g}^{-1}$  due to the activation process, and then decreased continuously. Without the PPy coating, the initial discharge capacity of the  $\text{V}_2\text{O}_5$  cathode was  $104.2 \text{ mAh}\cdot\text{g}^{-1}$  and then it rapidly decreased. The rate performance tests had shown that the specific discharge capacities of  $\text{V}_2\text{O}_5$ @PPy were 186.4, 139.1, 101.8 and  $65.3 \text{ mAh}\cdot\text{g}^{-1}$  at 0.5, 1, 2 and  $5 \text{ A}\cdot\text{g}^{-1}$ , respectively, while the specific discharge capacities of  $\text{V}_2\text{O}_5$ //Zn battery were much lower, 82.7, 58.2, 40 and  $30.7 \text{ mAh}\cdot\text{g}^{-1}$ , respectively. The EIS spectra had shown that the charge transfer resistance of the  $\text{V}_2\text{O}_5$ @PPy cathode was 260 Ohm compared to 274 Ohm for the  $\text{V}_2\text{O}_5$  cathode. Therefore, although the effect of PPy coating was not so pronounced as in other works [16,64], the cyclic stability, rate performance, ion and electron transfer rate of  $\text{V}_2\text{O}_5$  cathode were enhanced by the PPy coating.

Other vanadium oxides have also been considered for polymer-modified cathodes for AZIBs.  $\text{VO}_2$  seemed to be a suitable candidate owing to its various crystal structures. In [16], tetragonal  $\text{VO}_2$  hollow spheres were synthesized via a hydrothermal approach and a layer of polypyrrole was coated on their surface using ammonium persulfate as an oxidant and p-toluenesulfonic acid as a dopant through an ice bath route at  $5^\circ\text{C}$ . Compared to  $\text{VO}_2$ , the specific capacity of  $\text{VO}_2$ @PPy composites had increased almost twice (from  $231 \text{ mAh}\cdot\text{g}^{-1}$  to  $400 \text{ mAh}\cdot\text{g}^{-1}$ ), and cyclic stability had also improved well.  $\text{Zn}^{2+}$  diffusion coefficient values during insertion and extraction process were calculated to be  $10^{-6}$ – $10^{-8}$   $\text{cm}^2\text{s}^{-1}$ . The assembled battery cell presented the energy density of  $316.8 \text{ Wh}\cdot\text{kg}^{-1}$  at a power density of  $71.7 \text{ W}\cdot\text{kg}^{-1}$ . Ex situ XRD was used to study the structural evolution of the  $\text{VO}_2$ -5@PPy electrode at different stages of charge/discharge (Figure 5a). Initially, the characteristic peaks of  $\text{VO}_2$ -5@PPy were observed. Additional peaks of  $\text{Zn}_3(\text{VO}_4)_2$  appeared during the reaction due to the insertion and extraction of  $\text{Zn}^{2+}$ . During the discharge,  $2\theta$  values shifted to higher angles due to immersion into the electrolyte and the insertion of water molecules, expanding the interlayer space. During the charging process, the opposite shift was observed.  $\text{V}_2\text{O}_5\cdot\text{H}_2\text{O}$  characteristic peaks appeared in the pattern as a result of  $\text{VO}_2$  oxidation. The change in lattice fringe at (110) planes during the discharging/charging process of  $\text{VO}_2$ -5@PPy was studied by TEM (Figure 5b–e). While the morphologies of the composite did not change, the d value of (110) plane enlarged to 0.58 nm at the fully discharged state and recovered to the near-to-original 0.53 nm in the charged state, demonstrating effective intercalation/deintercalation of  $\text{Zn}^{2+}$  within the host structure of  $\text{VO}_2$ .

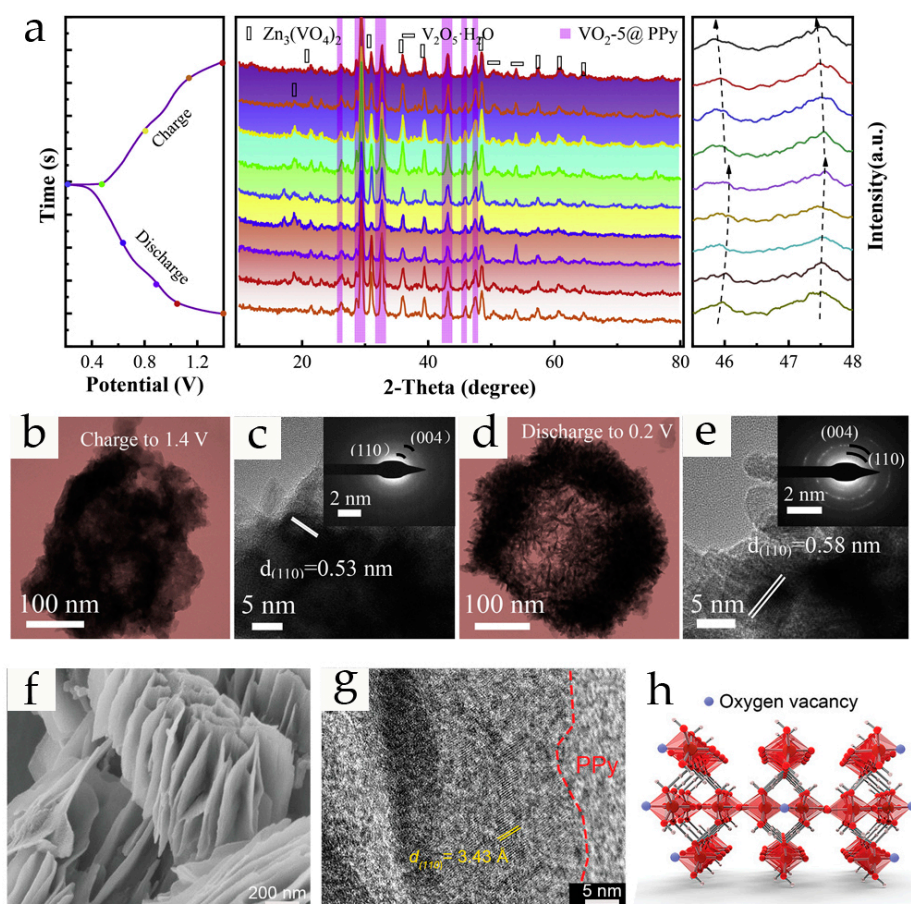


**Figure 5.** (a) Ex situ XRD patterns of VO<sub>2</sub>-5@PPy electrode at various charge/discharge states [16]; (b,c) TEM and HRTEM images of VO<sub>2</sub>-5@PPy charging at 1.4 V [16]; (d,e) TEM and HRTEM images of VO<sub>2</sub>-5@PPy discharging at 0.2 V [16]; (f) FESEM image of Od-HVO@PPy nanosheets [68]; (g) HRTEM image of Od-HVO@PPy [68]; (h) Crystal structure of the Od-VO<sub>2</sub>·xH<sub>2</sub>O [68].

In [68], oxygen deficient hydrate vanadium dioxide with PPy coating (O<sub>d</sub>-HVO@PPy) was synthesized by an in situ polymerization at pH 1–2. Pyrrole monomer worked both as a reactant and structure-directing agent; its polymerization was not only accompanied by the reduction of V<sub>2</sub>O<sub>5</sub> to HVO, but it determined the growth of crystals. The in situ polymerization resulted in PPy-coated VO<sub>2</sub>·xH<sub>2</sub>O (HVO), and then the O<sub>d</sub>-HVO@PPy nanosheets were obtained after the solution of HVO@PPy was quickly freeze-dried at 0.01 mbar vacuum at –85 °C. As seen from the SEM image, parallel-stacked nanosheets of HVO were obtained, and the PPy layer encapsulating HVO was observed by TEM. According to TGA, the PPy content in O<sub>d</sub>-HVO@PPy was 9 wt. %. The oxygen-deficient structure of O<sub>d</sub>-HVO@PPy was confirmed by XPS. The rate capability of the O<sub>d</sub>-HVO@PPy was studied at current densities from 0.1 to 10 A·g<sup>-1</sup>, and the O<sub>d</sub>-HVO@PPy delivered the reversible specific capacities of 346.5, 349.3, 340.4, 328.2, 316.7, 298.7, 277.4, 252.6 and 206 mAh·g<sup>-1</sup> at 0.1, 0.2, 0.4, 0.6, 1.0, 2.0, 4.0, 6.0 and 10 A·g<sup>-1</sup>, respectively. When the current density was returned to 0.1 A·g<sup>-1</sup>, the 91% capacity retention was observed. The O<sub>d</sub>-HVO@PPy delivered an energy density of 223 Wh·kg<sup>-1</sup> at a relatively low power density (67.6 W·kg<sup>-1</sup>), while still retaining 184 Wh·kg<sup>-1</sup> energy density when the power density was 1345 W·kg<sup>-1</sup>.

The increased layer spacing after the insertion of PPy is beneficial to the increase of the zinc ions transfer rate. PPy effectively improves conductivity and the long-term cycling performance of cathodes. In addition, due to the  $\pi$ -conjugated structure, PPy can shield Zn<sup>2+</sup> ions from electrostatic interactions with the oxygen atoms of the host material. PPy-coating inhibits the dissolution of the vanadium oxide in aqueous electrolyte.

### 2.3. Poly(3,4-Ethylenedioxythiophene)-Modified Vanadium-Based Cathodes

Poly(3,4-ethylenedioxythiophene) (PEDOT) is a polythiophene derivative with two alkoxy substituents attached to the 3 and 4 positions of the thiophene ring. The electron-donating oxygen substituents stabilize free radicals and positive electronic charges within the conjugated backbone, while the six-membered ring extends stabilization. As a result, PEDOT exhibits high stability in the doped state and excellent conductivity [90,91]. PEDOT, having displayed greatly enhanced stability compared to polypyrrole and polyaniline, has attracted extreme interest for energy applications in recent years [57,65,92,93]. PEDOT-intercalated materials have demonstrated high rate capability and cycle life in Li-ion batteries and supercapacitors. Poly(3,4-ethylenedioxythiophene)–polystyrene sulfonate (PEDOT:PSS) dispersion is also a popular choice for different applications due to its tunable conductivity, good electrochemical performance and processability. It has been reported that pure PEDOT plays a relatively small role in capacity contribution (24–30 mAh·g<sup>-1</sup>) [87,94] and may demonstrate pronounced capacity fading [89]. The key role of PEDOT is to create oxygen vacancies and to simultaneously form a conductive coating to improve the overall conductivity and protect the host material [70].

In [95] the V<sub>2</sub>O<sub>5</sub>/PEDOT composite was synthesized by the soft reduction of commercial V<sub>2</sub>O<sub>5</sub> by EDOT under microwave radiation. The resulting product had a layered structure (Figure 6a) and was identified by XRD as V<sub>10</sub>O<sub>24</sub>·12H<sub>2</sub>O monoclinic phase. The O to V atomic ratio obtained from XPS analysis confirmed that V<sup>5+</sup> ions were partially reduced to V<sup>4+</sup> during oxidation of EDOT. The ~8 wt. % content of PEDOT on the vanadium oxide surface was determined by TGA. The V<sub>2</sub>O<sub>5</sub>/PEDOT material provided high specific capacity 380 mAh·g<sup>-1</sup> at 0.3 A·g<sup>-1</sup>, and improved C-rate capability up to 20 A·g<sup>-1</sup> (Figure 6b). The capacity values for V<sub>2</sub>O<sub>5</sub>/PEDOT were 390, 381, 357, 326, 274, 192, 137, 101 mAh·g<sup>-1</sup> at 0.3, 0.5, 1, 2, 5, 10, 15, 20 A·g<sup>-1</sup>, respectively. The material was quite stable during long-term cycling. At 1 A·g<sup>-1</sup>, the specific capacity of V<sub>2</sub>O<sub>5</sub>/PEDOT demonstrated an increase associated with the activation process and stabilized after the 20th cycle (Figure 6c). The enhanced performance of V<sub>2</sub>O<sub>5</sub>/PEDOT in the ZnSO<sub>4</sub> electrolyte, due to the mixed valence state of vanadium, increased electronic and ionic conductivity, and decreased structural instability of the material during Zn<sup>2+</sup> intercalation, allowed the obtaining of capacity values which outperformed several PANI-modified V<sub>2</sub>O<sub>5</sub>-based electrodes, both polymer-coated and pre-intercalated [63,76,81].

In [66], the electrical conductivity of V<sub>2</sub>O<sub>5</sub> and VO@PEDOT composite was determined using impedance measurements with blocking electrodes. The conductivity of the VO@PEDOT sample (9.28 × 10<sup>-4</sup> S cm<sup>-1</sup>) was four times higher than that of V<sub>2</sub>O<sub>5</sub> (2.3 × 10<sup>-4</sup> S cm<sup>-1</sup>). The kinetics of the electrode processes in VO@PEDOT were investigated by EIS. In agreement with enhanced capacity values, the VO@PEDOT electrode also had a lower R<sub>ct</sub> value (2.2 Ohm, compared to 9.2 Ohm for V<sub>2</sub>O<sub>5</sub>), which explains the facilitation of charge transport and hence can increase the capacity values of this material. The analysis of the Warburg constant values (σ<sub>w</sub>) for the studied systems had shown that the apparent diffusion coefficient for VO@PEDOT should be ca. 30 times as large as for V<sub>2</sub>O<sub>5</sub>, thus confirming the faster ion intercalation process for the VO@PEDOT electrode. Furthermore, in [66], the comparative study of the dissolution of the V<sub>2</sub>O<sub>5</sub>- and VO@PEDOT-based cathodes with PVDF binder in the 3 M ZnSO<sub>4</sub> electrolyte was performed to estimate the stability of the materials under conditions where no electrochemical processes occur. The results of the AES-ICP analysis of vanadium content in the electrolyte had shown a sluggish rate of VO@PEDOT composite dissolution. After six months, only 6.53 mg·dm<sup>-3</sup> of vanadium species was detected in the electrolyte solution where VO@PEDOT electrode was soaked, whereas the concentration of dissolved vanadium species for the V<sub>2</sub>O<sub>5</sub> electrode was one order higher (57.8 mg·dm<sup>-3</sup>). Thus, it was shown that the inclusion of PEDOT in the VO@PEDOT material structure inhibits vanadium oxide dissolution not only during charge-discharge cycling, but also at stationary conditions, which is beneficial for its use in commercial devices as it can provide long shelf life for batteries.

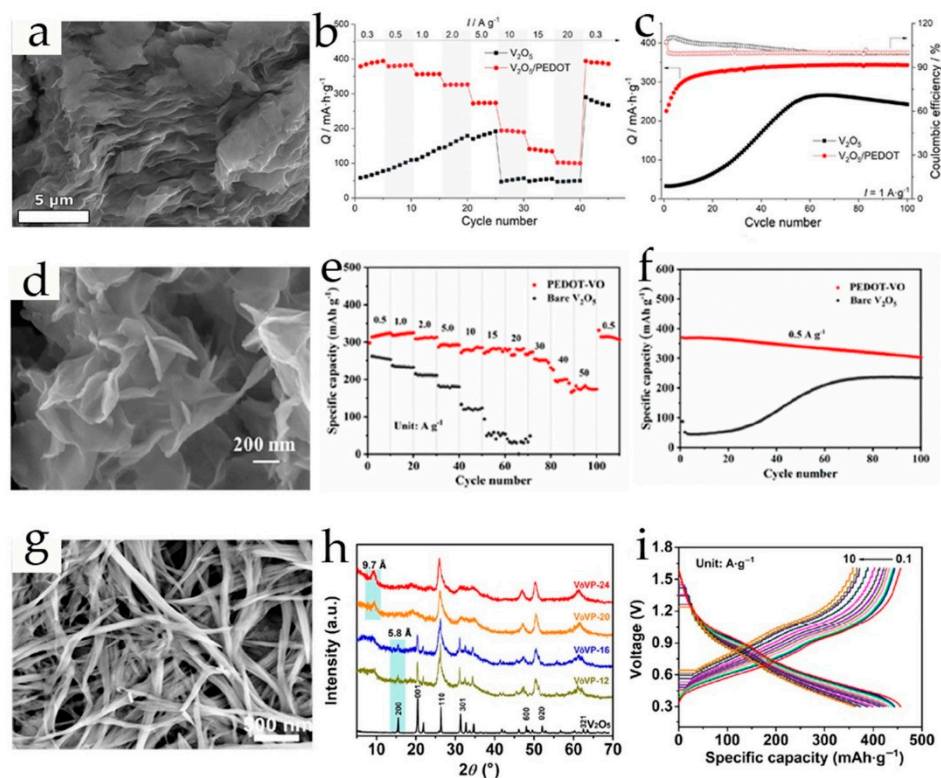


**Figure 6.** (a) SEM image of  $V_2O_5/PEDOT$  [95]; (b) C-rate capability of  $V_2O_5/PEDOT$  [95]; (c) Electrochemical performance of  $V_2O_5$  and  $V_2O_5/PEDOT$  electrodes: cycle performance and coulombic efficiency at  $1 A g^{-1}$  [95]; (d) Typical SEM images of PEDOT-VO [65]; (e) Rate performance of PEDOT-VO and  $V_2O_5$  electrodes at different current densities [65]; (f) Cycle performance of PEDOT-VO and  $V_2O_5$  electrodes at  $0.5 A g^{-1}$  [65]; (g) SEM of the as-prepared VöVP-20 [89]; (h) XRD patterns of VöVP-12, VöVP-16, VöVP-20, VöVP-24 and commercial  $V_2O_5$  [89]; (i) GCD curves of VöVP-20 at different rates [89].

PEDOT-intercalated vanadium oxide (PEDOT-VO), with  $V^{5+}/V^{4+}$  mixed valence states, was obtained in [65]. First, EDOT was intercalated into the  $V_2O_5$  material during continuous mixing and was then polymerized using a hydrothermal method. PEDOT-VO 3D-flowers composed of nanosheets can be clearly seen on the SEM images (Figure 6d). The content of PEDOT in PEDOT-VO composite was estimated as 10.08 wt. % by TGA. Compared to pristine  $V_2O_5$ , the electrical conductivity and the reaction kinetics of the PEDOT-VO composite were improved due to the intrinsic conductivity of PEDOT and mixed valence states of vanadium. The electrical conductivities of  $V_2O_5$  and PEDOT-VO were  $6.79 \times 10^{-6} S \cdot cm^{-1}$  and  $1.17 \times 10^{-4} S \cdot cm^{-1}$ , respectively. The important evidence of fast kinetics of charge transport in PEDOT-VO composite is its high rate capability; it maintained the specific capacity of  $175 mA h g^{-1}$  at the current density of  $50 A \cdot g^{-1}$  (Figure 6e). The PEDOT-VO cathodes showed short activation time and delivered a high specific capacity of  $370.5 mA h g^{-1}$  at  $0.5 A g^{-1}$  and 96.9% capacity retention after 1000 cycles at  $5.0 A g^{-1}$  (Figure 6f).

After it was demonstrated that an oxygen-deficient PEDOT- $NH_4V_3O_8$  cathode material could achieve improved electrochemical performance as compared to pristine  $NH_4V_3O_8$  [87], this approach was applied to  $V_2O_5$ . The introduction of PEDOT into  $V_2O_5$  contributed to the formation of oxygen vacancies and led to an enlarged interlayer spacing in [89]. For the synthesis of oxygen-deficient  $V_2O_5$ -PEDOT (VöVP), commercial  $V_2O_5$  powder dispersed in water was mixed with different amounts of EDOT and continuously stirred for 6 days at room temperature to obtain VöVP with various concentrations of Vö. Thus, the PEDOT was formed via the oxidative polymerization of EDOT monomer, which was simultaneously intercalated into the  $V_2O_5$ -layered structure. After PEDOT intercalation, Vö were formed, with an expansion in the interlayer spacing of  $V_2O_5$ . The XPS analysis indicated that the Vö

concentration in samples was controlled by the amount of EDOT monomer added during the synthesis process, and ranged from 12 to 24%. The as-prepared VöVP-20 sample had a nanobelt structure, with ca. 30 nm in width and several micrometers in length (Figure 6g). The XRD spectra of all VöVP samples revealed the presence of pure  $V_2O_5$ , suggesting that  $V_2O_5$  remained unchanged by the polymerization of EDOT. The peak intensity of VöVP decreased with the increase in the PEDOT content, suggesting that some of the diffraction peaks in VöVP were masked by PEDOT (Figure 6h). The GCD curves of VöVP-20 at various current densities showed small polarization (Figure 6i). The specific capacities of the sample with 20% of Vö (VöVP-20), which had shown the best performance, were 444, 449, and 358  $\text{mAh}\cdot\text{g}^{-1}$  at 0.1, 0.2, and 10.0  $\text{A}\cdot\text{g}^{-1}$ , respectively. The cathode also exhibited an excellent cyclical performance of 94.3% after 6000 cycles. The high symmetry of the discharge/charge curves in GITT confirmed a highly reversible  $\text{Zn}^{2+}$  storage mechanism. The  $D_{\text{Zn}}$  of VöVP-20 is in the magnitude range of  $10^{-8}$ – $10^{-9}$   $\text{cm}^2\cdot\text{s}^{-1}$ .

As  $V_2O_5$ -PEDOT had shown improved and stable performance as a cathode for ZIBs [89] it was tested in cells with copper-coated Zn anode (Cu–Zn) [96].  $V_2O_5$ -PEDOT was synthesized based on the described method, and full batteries with Zn or Cu–Zn anodes and  $V_2O_5$ -PEDOT cathodes were assembled and tested. The  $V_2O_5$ -PEDOT//Cu–Zn demonstrated superior performance compared to the  $V_2O_5$ -PEDOT//Zn battery. The specific capacity of  $V_2O_5$ -PEDOT//Cu–Zn at 0.1, 0.2, 0.5, 1, 2, 3, 4, 5  $\text{A}\cdot\text{g}^{-1}$  was of 323, 311, 266, 246, 227, 215, 205, 195  $\text{mAh}\cdot\text{g}^{-1}$ , respectively, while the  $V_2O_5$ -PEDOT//Zn battery showed a capacity of 284, 255, 231, 223, 211, 201, 194, 187  $\text{mAh}\cdot\text{g}^{-1}$ , respectively. The long-term cycling tests at 5  $\text{A}\cdot\text{g}^{-1}$  have shown that both cells underwent an increase in capacity due to the activation of  $V_2O_5$  during the first 60 cycles, and  $V_2O_5$ -PEDOT//Zn suffered from a capacity fade after 120 cycles, probably due to the formation of zinc dendrites resulting in “dead Zn” and the increased internal resistance of the batteries. In contrast,  $V_2O_5$ -PEDOT//Cu–Zn showed a stable cycling performance over 1000 cycles. This example demonstrates the role of full cell composition on the performance of the cathodes and the routes for further investigations.

In [97], a binder-free composite cathode based on carbon nanotubes and PEDOT-intercalated  $V_2O_5$  was obtained. The fabrication of the PVO/PEDOT/CNTs composites was realized via a high-energy ball-milling technique in water solution using  $V_2O_5$ , EDOT, and CNTs as precursors. During mechanochemical reaction under wet ball-milling, the polymerization of EDOT at both the interlayer and surface of  $V_2O_5$ , the peeling of thin PEDOT-intercalated  $V_2O_5$  nanoflakes, the shortening of CNTs, and the in situ self-assembly of the intermediate products occurred simultaneously. The PVO/PEDOT/CNTs cathode demonstrated the average discharge capacities of 440.6, 428.6, 415.2, 403.4, 380.4, 350.6, 330.3, 289.4, and 245.2  $\text{mAh}\cdot\text{g}^{-1}$  at current densities of 0.5, 1, 2, 3, 5, 8, 10, 15, and 20  $\text{A}\cdot\text{g}^{-1}$ , respectively. At a high current density of 30  $\text{A}\cdot\text{g}^{-1}$ , the cathode maintained a discharge capacity of 180.0  $\text{mAh}\cdot\text{g}^{-1}$ , implying that the battery can be fully discharged and charged within 60 s, which is desirable for high energy/power density applications. The PVO/PEDOT/CNTs cathode maintained high energy density of 125.2  $\text{Wh}\cdot\text{kg}^{-1}$  at a power density of 10,222.8  $\text{W}\cdot\text{kg}^{-1}$ . The energy densities of the Zn//PVO/PEDOT/CNTs battery leave behind most of the recently reported AZIBs based on vanadium-based cathode materials, such as PVO nanosheets [60], PANI/ $V_2O_5$  sponge [54],  $\text{O}_d$ –HVO@PPy [68], shallow-layer PEDOT-intercalated  $V_2O_5$  [57] and PEDOT-modified ammonium vanadate nanofibers [58].

PEDOT:PSS was introduced into  $V_2O_5\cdot 3\text{H}_2\text{O}$  during one-step hydrothermal synthesis in [92]. The X-ray diffraction pattern of obtained P-VO corresponded to the diffraction peaks of pure-phase  $V_2O_5\cdot 3\text{H}_2\text{O}$ . The interlayer spacing of  $V_2O_5\cdot 3\text{H}_2\text{O}$  (11.8 Å) was enlarged to 12.9 Å for P-VO. The TG analysis revealed ~1.3% weight content of PEDOT:PSS. XPS analysis revealed that the addition of PEDOT:PSS into the composite increased the ratio of  $\text{V}^{4+}$  to  $\text{V}^{5+}$ , indicating more oxygen vacancies. The P-VO cathode demonstrated a stable rate performance at all used current densities (0.2–10.0  $\text{A}\cdot\text{g}^{-1}$ ), superior to that of the unmodified VO cathode. The P-VO cathode demonstrated good long-term durability under different current densities

and 100% Coulombic efficiency throughout all cycles. The increase of the specific capacity from the initial value of  $247.9 \text{ mAh}\cdot\text{g}^{-1}$  to  $302.0 \text{ mAh}\cdot\text{g}^{-1}$  after 800 cycles at  $5.0 \text{ A}\cdot\text{g}^{-1}$  was observed, which is related to the activation of the cathode material and wetting by the electrolyte. The diffusion coefficient ( $D_{\text{Zn}}$ ) of P-VO obtained by the GITT technique decreased slightly with  $\text{Zn}^{2+}$  intercalation/deintercalation, and most of the  $D_{\text{Zn}}$  values were in range of  $10^{-8}$  to  $10^{-10} \text{ cm}^2\cdot\text{s}^{-1}$  over the entire intercalation/deintercalation process. The fast kinetics of P-VO were also confirmed by the EIS. The charge transfer resistance of P-VO was 45.1 Ohm, as compared to unmodified VO (199.8 Ohm), and decreased for both P-VO (9.0 Ohm) and VO (114.9 Ohm) after 50 cycles at  $2.0 \text{ A}\cdot\text{g}^{-1}$ .

In [98] 3,4-ethylenedioxythiophene was pre-intercalated into the layered vanadium oxide and then polymerized in the interlamellar space. The resulting 2D PEDOT-intercalated  $\text{V}_2\text{O}_5$  aerogel (PEDOT/ $\text{V}_2\text{O}_5$ ) was obtained based on the template effect through freeze-drying. The XRD results confirmed that the interlayer distance significantly expanded as the monomer molecules intercalated and polymerized in situ between the V-O layers. The PEDOT/ $\text{V}_2\text{O}_5$  cathode delivered reversible capacities of 247, 229, 218, 209, 197, 187, 179, 169 and  $154 \text{ mAh}\cdot\text{g}^{-1}$  at 0.2, 0.5, 1, 2, 5, 10, 20, 30 and  $50 \text{ A}\cdot\text{g}^{-1}$ , respectively, in which the PEDOT component provided a negligible capacity. The PEDOT/ $\text{V}_2\text{O}_5$  cathode demonstrated a good high-rate performance ( $154 \text{ mAh}\cdot\text{g}^{-1}$  at  $50 (!) \text{ A}\cdot\text{g}^{-1}$ ) and excellent cycling stability at high current densities (88% capacity retention at  $10 \text{ A}\cdot\text{g}^{-1}$ ). The  $\text{Zn}^{2+}$  ion diffusion coefficients in the PEDOT/ $\text{V}_2\text{O}_5$  composite estimated by GITT were  $10^{-9}$ – $10^{-8} \text{ cm}^2\cdot\text{s}^{-1}$ . The enhanced ion diffusion in the composite is related to the sufficient interlayer spacing enabled by PEDOT intercalation as well as the ultrathin 2D sheet morphology with more exposed  $\text{Zn}^{2+}$  insertion sites and shorter ion diffusion paths. A high specific energy of  $216 \text{ Wh}\cdot\text{kg}^{-1}$  was delivered by the PEDOT/ $\text{V}_2\text{O}_5$  cathode at a low power density ( $252 \text{ W}\cdot\text{kg}^{-1}$ ). The specific energy was  $112 \text{ Wh}\cdot\text{kg}^{-1}$ , even at an ultrahigh power density of  $35.8 \text{ kW}\cdot\text{kg}^{-1}$ , which is superior to most of the reported vanadium-based cathodes.

A shallow-layer pillaring strategy was proposed in [57]. The interlayers of  $\text{V}_2\text{O}_5$  grains were expanded with a conducting polymer only at the shallow-layer positions, instead of the nanostructuring strategy. The  $\text{V}_2\text{O}_5$ @PEDOT (VOP) sample was synthesized via a one-pot self-polymerization method by stirring  $\text{V}_2\text{O}_5$  powder and the EDOT monomer for one week. The preservation of bulk  $\text{V}_2\text{O}_5$  peaks on the XRD patterns of  $\text{V}_2\text{O}_5$ @PEDOT indicated the shallow-layer intercalation of PEDOT at the oxide surface, while a new peak appeared at  $2\theta 8.96^\circ$  after EDOT insertion. The content of PEDOT in VOP was estimated to be 22.1 wt. % by TGA. It was demonstrated that PEDOT suppressed the dissolution of  $\text{V}_2\text{O}_5$  particles, reinforced the conductive contact between grains and boosted the pseudocapacitive contribution (467%) and  $\text{Zn}^{2+}$  diffusion coefficient ( $1.43 \times 10^{-9}$ – $1.81 \times 10^{-8} \text{ cm}^2\cdot\text{s}^{-1}$ ). The composite VOP cathode was tested at high current densities and delivered reversible capacities as high as 360, 338, 280, 222, and  $197 \text{ mAh}\cdot\text{g}^{-1}$  at current densities of 1, 2, 5, 8, and  $10 \text{ A}\cdot\text{g}^{-1}$ , respectively. High energy densities of 280.2 and  $205.8 \text{ Wh}\cdot\text{kg}^{-1}$  and high power densities of 0.70 and  $5.96 \text{ kW}\cdot\text{kg}^{-1}$  were calculated for VOP at 1 and  $10 \text{ A}\cdot\text{g}^{-1}$ , respectively. It was suggested that the approach of shallow-layer pillaring can be extended to more electrode systems.

$\text{V}_2\text{O}_5$ @PEDOT hybrid core/shell nanosheet arrays have been grown on a carbon cloth (CC) substrate in [70] through a three-step process. On the third step, a PEDOT film with a thickness of  $\approx 5 \text{ nm}$  was uniformly grown on the  $\text{V}_2\text{O}_5$  nanosheet arrays by electrodeposition at a constant current density to form the binder-free  $\text{V}_2\text{O}_5$ @PEDOT/CC electrode. The initial capacity of the  $\text{V}_2\text{O}_5$ @PEDOT/CC cathode was  $360 \text{ mAh}\cdot\text{g}^{-1}$  at  $0.1 \text{ A}\cdot\text{g}^{-1}$ . The high rate capability with a specific capacity of  $232 \text{ mAh}\cdot\text{g}^{-1}$  at  $20 \text{ A}\cdot\text{g}^{-1}$ , and 89% capacity retention (after 1000 cycles at  $5 \text{ A}\cdot\text{g}^{-1}$ ), was observed for  $\text{V}_2\text{O}_5$ @PEDOT/CC. The enhanced electrochemical performance of the  $\text{V}_2\text{O}_5$ @PEDOT resulted from the synergistic effects of the  $\text{V}_2\text{O}_5$  nanosheet network structure and the conducting PEDOT shell, improving ion and electron transport kinetics. The Zn// $\text{V}_2\text{O}_5$ @PEDOT/CC battery delivered energy and power densities of  $243 \text{ Wh}\cdot\text{kg}^{-1}$  and  $18\,000 \text{ W}\cdot\text{kg}^{-1}$ , respectively.

In [99], ultrathin  $\text{VO}_2$ -PEDOT hybrid nanobelts comprising  $\text{VO}_2$  and poly(3,4-ethylenedioxythiophene) were synthesized by a modified two-step process including the successive in-

tercalation of EDOT monomers into the layered  $V_2O_5$  at room temperature followed by the reduction of the obtained  $V_2O_5$ /PEDOT composite hydrothermally to convert it into  $VO_2$ -PEDOT. The TGA results indicated that the content of the polymer in the  $VO_2$ -PEDOT nanobelts was about 19.2 wt. %. The single crystalline structure of ultrathin  $VO_2$  nanobelts and a discrete conducting PEDOT layer resulted in good compatibility of the composite with the electrolyte, and good ionic and electronic conductivity. Simultaneous proton and  $Zn^{2+}$  co-intercalation was proposed as an energy storage mechanism for  $VO_2$ -PEDOT cathode in the  $Zn(CF_3SO_3)_2$  electrolyte. The discharge capacities of the  $VO_2$ -PEDOT cathode at 0.5, 1, 2, 3, 5, 8 and 10  $A \cdot g^{-1}$  were 448.5, 430.4, 406.2, 389.4, 347.2, 280.2, and 231.2  $mAh \cdot g^{-1}$ , respectively, due to high reversibility and fast carrier migration in the  $VO_2$ -PEDOT electrode. The migration kinetics of Zn ions in the  $VO_2$ -PEDOT cathode were investigated by the GITT, and the  $Zn^{2+}$  diffusion coefficient was of  $10^{-8}$  to  $10^{-9} \text{ cm}^2 \cdot \text{s}^{-1}$ , indicating fast  $Zn^{2+}$  transport in the  $VO_2$ -PEDOT electrode.

PEDOT has also been successfully introduced into the interlayers of ammonium vanadate [58,87] and sodium vanadate [100]. PEDOT-intercalated  $NH_4V_3O_8$  (PEDOT-NVO) was obtained in [87] by in situ intercalative polymerization (Figure 7a). PEDOT-NVO presents a connected nanobelt structure which retains the general morphology of pristine NVO (Figure 7b). The intercalation of PEDOT not only expanded the interlayer spacing of NVO (from 7.8 to 10.8 Å) (Figure 7c), enhancing the  $Zn^{2+}$  mobility within the interlayer, but also promoted the formation of oxygen vacancies in the PEDOT-NVO. This conclusion was supported by DFT calculations. A PEDOT-reinforced layered structure of PEDOT-NVO with low kinetic energy barrier enabled fast  $Zn^{2+}$  diffusion and long cycle life of the cathode (capacity retention of 94.1% after 5000 cycles). The discharge capacity PEDOT-NVO was higher than that of pristine NVO (Figure 7d) and it demonstrated the capacity retention of 80.8% after 1000 cycles at 1  $A \cdot g^{-1}$ .

A facile sonochemical method for controlling the interlayer structure of ammonium vanadate (Figure 7e) nanofibers (AVNF) using poly(3,4-ethylenedioxythiophene) was suggested in [58]. The novel PEDOT-intercalated AVNF composite cathode (E-AVNF) had demonstrated improved rate capability and electrochemical reversibility as well as cycle stability. E-AVNF exhibited the specific capacity of 344, 326, 315, 306, 287, 272, 248, 227, and 210  $mAh \cdot g^{-1}$  at the current densities of 0.5, 1, 1.5, 2, 3, 4, 6, 8, and 10  $A \cdot g^{-1}$ , respectively, and also a high capacity of 155  $mAh \cdot g^{-1}$  at an extremely high current density of 20  $A \cdot g^{-1}$ , which demonstrated the excellent rate capability of E-AVNF (Figure 7f). PEDOT provided many conductive channels inside the vanadate layers, enabling E-AVNF to maintain a high capacity at a high current density. The high electrical conductivity of E-AVNF ( $4.1 \times 10^{-2} \text{ S} \cdot \text{cm}^{-1}$ ) facilitated faster charge transfer in the electrode. The excellent cycle stability of E-AVNF can be explained by the fact that the intercalated PEDOT acts as a more substantial “pillar” than the  $NH_4^+$  ion in the vanadate layer. E-AVNF delivered a high energy density of 124  $Wh \cdot kg^{-1}$  at the power density of 16 000  $W \cdot kg^{-1}$ . The charge transfer resistance of E-AVNF (20.7 Ohm) was lower than that of AVNF (26.3 Ohm), indicating the faster reaction kinetics of E-AVNF (Figure 7g). These results demonstrate that the intercalated PEDOT improved the reaction kinetics of vanadate nanofibers. The diffusion behavior of  $Zn^{2+}$  ions in E-AVNF was studied by GITT. The calculated diffusion coefficient of  $Zn^{2+}$  ions for E-AVNF during discharging and charging was  $3.73 \times 10^{-9}$  and  $2.30 \times 10^{-9} \text{ cm}^2 \cdot \text{s}^{-1}$ , respectively, compared to  $1.03 \times 10^{-9}$  and  $5.95 \times 10^{-10} \text{ cm}^2 \cdot \text{s}^{-1}$  for AVNF, respectively, indicating that  $Zn^{2+}$  ions can migrate more easily and quickly inside the vanadate layers of E-AVNF than those of AVNF due to the enlarged interlayer spacing. The diffusion coefficients of  $Zn^{2+}$  ions are lower during the de-intercalation (charge) process than during the intercalation (discharge) process because of the difficulty of  $Zn^{2+}$  extraction, which may be responsible for E-AVNF capacity fading.

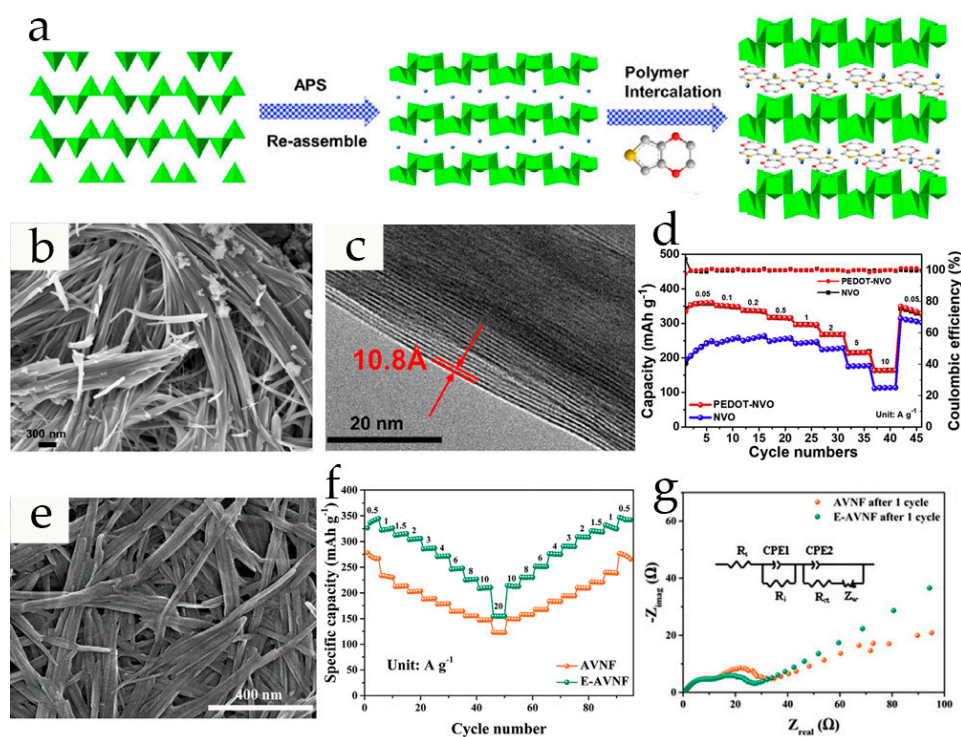


**Figure 7.** (a) Scheme of structural changes during the preparation of PEDOT-NVO [87]; (b) SEM of PEDOT-NVO [87]; (c) HRTEM of PEDOT-NVO [87]; (d) Rate capability of NVO and PEDOT-NVO at different current densities [87]; (e) SEM image of E-AVNF [58]; (f) Nyquist plots of AVNF and E-AVNF after 1st cycle [58]; (g) Specific capacities of AVNF and E-AVNF electrodes at different current densities [58].

In order to overcome the sluggish  $\text{Zn}^{2+}$  diffusion kinetics, bridge-oxygen sited oxygen vacancies were introduced into sodium vanadate  $\text{Na}_{0.76}\text{V}_6\text{O}_{15}$  (NVO) through the in situ vapor polymerization of 3,4-ethylenedioxythiophene [100]. In a vacuum reactor, with NVO acting as oxidant, vapored EDOT in situ oxidatively polymerized and chemically bonded with NVO via the sulfur cations in PEDOT and the oxygen anions in NVO, forming a nanocable-structured oxygen-vacancy rich NVO/PEDOT (Vö-PNVO). The oxygen vacancies and accompanying  $\text{V}^{4+}$  were generated in Vö-PNVO in the non-oxygen atmosphere. The Vö-PNVO exhibited high-rate capability with capacities of 256, 234, 228, 224, 221, 205 and 165  $\text{mAh}\cdot\text{g}^{-1}$  at 0.1, 0.2, 0.4, 0.8, 1, 2 and 4  $\text{A}\cdot\text{g}^{-1}$ , respectively, and the capacity almost recovered when the current density was switched back to 0.05  $\text{A}\cdot\text{g}^{-1}$ . The improved capacity, rate performance and enhanced energy efficiency of Vö-PNVO are closely related to PEDOT and oxygen vacancies. The Vö-PNVO-based AZIBs exhibited energy-density/power-density values of 228  $\text{Wh}\cdot\text{kg}^{-1}/40 \text{ W}\cdot\text{kg}^{-1}$  and 105  $\text{Wh}\cdot\text{kg}^{-1}/3160 \text{ W}\cdot\text{kg}^{-1}$  at 0.05 and 4.0  $\text{A}\cdot\text{g}^{-1}$ , respectively. The  $\text{Zn}^{2+}$  diffusion coefficient of Vö-PNVO, calculated from GITT, was in the range  $10^{-14}$ – $10^{-13} \text{ cm}^2\cdot\text{s}^{-1}$ .

Rational design of the structure and morphology of the  $\text{V}_2\text{O}_5/\text{PEDOT}$  composites allows the optimization of the ion/electron transport in the materials, and conducting polymer shells provide abundant Zn-storage active sites, promote zinc ion/electron transport and serve as an elastic layer to inhibit structural breakdown during the insertion and extraction of zinc ions. The incorporation of PEDOT via an in situ chemical approach with the partial reduction of  $\text{V}_2\text{O}_5$  in the presence of an EDOT monomer may enhance the electrochemical performance by transformation of the initial structure into mixed-valence compounds in the resulting vanadium oxide/conducting polymer composite.

### 3. Conclusions and Outlook

As follows from the above discussion, conducting polymer-intercalated vanadium oxides have recently become a research hotspot due to their unique combination of properties, allowing the improvement of the electrochemical performance of AZIBs. The introduction of conducting polymers into vanadium-based cathode materials has proven to be an effective method for several reasons. First, it leads to enhanced electrical conductivity of composites, originating from the electronically conducting polymer molecules, intercalated into the layered vanadium oxide, and enlarged interlayer distances, which facilitate enhanced ionic diffusion. Moreover, co-/pre-intercalation of water molecules into layered oxide structures can lubricate the  $\text{Zn}^{2+}$  diffusion during the cycling process. Benefiting from the shielding effect, these interlamellar water molecules along with polymer molecules reduce the effective charge of  $\text{Zn}^{2+}$  and, hence, the interaction between intercalated metal ions and host lattice, enabling faster ion diffusion.

Second, conducting polymers can be used as shells on active grains for additional enhancement of conductivity, and can simultaneously protect the active material from direct contact with the electrolyte, suppressing the interfacial side reactions, and preventing the dissolution of the cathodes during the charge/discharge process. Furthermore, the polymer coating may help to maintain the integrity of the electrodes. All these factors will stabilize the host electrode material, facilitating prolonged charge–discharge cycling.

Third, the in situ polymerization of CPs induces the partial reduction of  $\text{V}^{5+}$  to  $\text{V}^{4+}$ , leading to the formation of oxygen vacancies in  $\text{V}_2\text{O}_5$ . The oxygen vacancies can alter the material surface chemistry, facilitating enhanced ionic diffusion [68]. The new mixed valence states can also improve the initial conductivity of layered oxides [11], which is reflected in the absence of so-called activation processes, and is characteristic for pristine unmodified vanadium oxide, providing better overall electrochemical performance [64].

To support the conclusions, the electrochemical performance of polymer-intercalated vanadium compounds is summarized for comparison in Table 1. From these studies, one can see that intercalation of PANI, PPy and PEDOT into host cathode materials can not only enlarge the interlayer spacing and create more open space for the reversible intercalation of ions, but in all cases also significantly improve the overall performance of AZIBs.

Although considerable progress has been achieved in composite vanadium oxide-based cathodes with conducting polymers as modifiers, some challenges still need to be further solved. In our view, the optimization of the material is essential for better performance of batteries. More research and development of new materials is needed to select optimized compositions and synthetic procedures, which could further improve the cathode materials.

Further steps to improve the efficiency of cathode materials for AZIBs can be made based on a deeper engineering of the interlayer space of vanadium oxides with a combination of two prospective approaches: pre-intercalation of vanadium oxides with metal ions and intercalation of conducting polymers. Both of these separately proposed approaches could result in a significant improvement of the electrochemical characteristics of vanadium oxide-based cathodes. The first attempts at the co-intercalation of conducting polymers and metal ions have recently been successful [101–103], and further studies of this novel route for the design of high-performance cathode materials for AZIBs are needed.

**Table 1.** Electrochemical performance of selected vanadium oxide-based composites with CPs as cathodes in AZIBs.

Material	Synthesis Method	Morphology/Interlayer Spacing, Å	Electrolyte	Specific Capacity, mAh g <sup>-1</sup> (Current Density, A·g <sup>-1</sup> )	Capacity Retention, (Number of Cycles and Current, A·g <sup>-1</sup> )	ΔE, V	Ref.
PANI-V <sub>2</sub> O <sub>5</sub> ·nH <sub>2</sub> O (PVO)	in situ oxidative/intercalative polymerization	rose-like/14.02	3 M Zn(CF <sub>3</sub> SO <sub>3</sub> ) <sub>2</sub>	420.4 (0.5); 400 (5); 288 (20)	87.5% (600, 5)	0.4–1.6	[53]
V <sub>2</sub> O <sub>5</sub> @PANI	chemical oxidation polymerization	uniform 3D porous	3 M Zn(CF <sub>3</sub> SO <sub>3</sub> ) <sub>2</sub>	361 (0.1); 283 (1); 201 (6)	93.8% (1000, 5)	0.3–1.6	[67]
PANI-V <sub>2</sub> O <sub>5</sub>	in situ hydrothermal reaction	13.9	3 M Zn(CF <sub>3</sub> SO <sub>3</sub> ) <sub>2</sub>	375.2 (1); 264.6 (10); 197.1 (20)	97.6% (2000, 20)	0.2–1.6	[60]
PANI-V <sub>2</sub> O <sub>5</sub>	one-pot hydrothermal method (140 °C)	nanosheets/14.2	3 M Zn(CF <sub>3</sub> SO <sub>3</sub> ) <sub>2</sub>	360 (0.5); 272 (5); 216 (10)	90% (2000, 5)	0.4–1.4	[76]
PANI-V <sub>2</sub> O <sub>5</sub>	one-pot hydrothermal method (120 °C)	nanosheets/14.2	3 M Zn(CF <sub>3</sub> SO <sub>3</sub> ) <sub>2</sub>	297 (0.5); 199 (5); 133 (10)	85% (100, 5)	0.4–1.4	[76]
PANI/V <sub>2</sub> O <sub>5</sub>	mild molecule-exchange reaction at room temperature	3D sponge-like morphology/13.82	3 M Zn(CF <sub>3</sub> SO <sub>3</sub> ) <sub>2</sub>	353.6 (0.1); 278 (4)	87.5% (100, 0.2)	0.2–1.5	[54]
PANI-VOH	interface-intercalation method	3D sponge-like morphology/14.1	3 M Zn(CF <sub>3</sub> SO <sub>3</sub> ) <sub>2</sub>	363 (0.1)	~49% (2000, 5)	0.2–1.5	[77]
PANI-VOH	low-temperature hydrothermal process	agglomerated corrugated nanosheets, porous/14.2	3 M Zn(CF <sub>3</sub> SO <sub>3</sub> ) <sub>2</sub> + 6 M LiTFSI (water-in-salt)	346 (0.3); 323 (1); 186 (1)	80% (800, 1)	0.4–1.6	[80]
(PANI) <sub>x</sub> V <sub>2</sub> O <sub>5</sub>	self-assembly process	3D network of nanosheets/13.9	3 M Zn(CF <sub>3</sub> SO <sub>3</sub> ) <sub>2</sub>	350 (0.1); 250 (1); 190 (5)	~90% (100, 0.1)	0.3–1.6	[63]
PANI/V <sub>2</sub> O <sub>5</sub>	hydrothermal method	nanosheets/13.67	2 M Zn(CF <sub>3</sub> SO <sub>3</sub> ) <sub>2</sub>	278 (0.5); 264 (1); 156 (10)	120.5% (100, 1)	0.4–1.4	[104]
PANI/V <sub>2</sub> O <sub>5</sub> (PVO)	hydrothermal method	aggregated flakes/14.1	2 M Zn(CF <sub>3</sub> SO <sub>3</sub> ) <sub>2</sub>	356 (0.1); ~290 (5); 235 (20)	96.3% (1000, 5)	0.3–1.6	[62]
(V <sub>2</sub> O <sub>5-x</sub> )/PANI	intercalation–polymerization method	2D nanosheet/15.6	2 M ZnSO <sub>4</sub>	490 (0.1); 234 (16)	71% (1000, 1)	0.4–1.6	[79]
NH <sub>4</sub> V <sub>3</sub> O <sub>8</sub> /PANI	one-step hydrothermal reaction	10.8	2 M Zn(CH <sub>3</sub> SO <sub>3</sub> F) <sub>2</sub>	397.5 (1); 300 (10)	95% (1000, 10)	0.4–1.6	[105]
PANI/V <sub>2</sub> O <sub>5</sub>	hydrothermal reaction	loosely aggregated nanosheets/14.2	2 M Zn(CF <sub>3</sub> SO <sub>3</sub> ) <sub>2</sub>	445 (0.1); 380 (0.5); 340 (1); 247 (2)	94% (100, 0.1); 80% (600, 2)	0.4–1.4	[106]
PPy-intercalated V <sub>2</sub> O <sub>5</sub>	hydrothermal reaction	foliated rock/12.38	3 M Zn(CF <sub>3</sub> SO <sub>3</sub> ) <sub>2</sub>	404 (0.1); 241 (5)	98% (2000, 10)	0.3–1.5	[86]
PPy/VOH	in situ intercalation	layered nanosheet/14.0	3 M Zn(CF <sub>3</sub> SO <sub>3</sub> ) <sub>2</sub>	383 (0.1); 303 (1); 281 (2)	72% (2000, 4)	0.2–1.5	[85]
V <sub>2</sub> O <sub>5</sub> -PPy	in situ polymerization at room temperature	fibrous nanobelts/6.9	3 M Zn(CF <sub>3</sub> SO <sub>3</sub> ) <sub>2</sub>	441 (0.1); 291 (5)	95.92% (2000, 5)	0.3–1.6	[64]
V <sub>2</sub> O <sub>5</sub> /PPy	in situ polymerization at room temperature	nanowires (cable-like)/9.6	3 M Zn(CF <sub>3</sub> SO <sub>3</sub> ) <sub>2</sub>	466 (0.1); 174 (5)	95% (1000, 5)	0.3–1.6	[81]
V <sub>2</sub> O <sub>5</sub> @PPy	in situ oxidation	grained/2.61	2 M ZnSO <sub>4</sub>	186.4 (0.5); 101.8 (1); 65.3 (5)	95.6% (300, 1)	0.2–1.8	[39]
VO <sub>2</sub> @PPy	hydrothermal process at 5 °C	hollow nanospheres/5.6	3 M Zn(CF <sub>3</sub> SO <sub>3</sub> ) <sub>2</sub>	440 (0.1); 330 (1)	~48% (860, 1)	0.2–1.4	[16]
O <sub>d</sub> -HVO@PPy	in situ polymerization	nanosheets/3.43	2 M ZnSO <sub>4</sub>	346 (0.1); 206 (10)	85% (500, 2); 77% (1000, 10)	0.2–1.6	[68]
V <sub>2</sub> O <sub>5</sub> /PEDOT	microwave-assisted in situ polymerization	nanosheets	3 M ZnSO <sub>4</sub>	390 (0.3); 274 (5); 102 (20)	93% (200, 5)	0.3–1.4	[95]

Table 1. Cont.

Material	Synthesis Method	Morphology/Interlayer Spacing, Å	Electrolyte	Specific Capacity, mAh g <sup>-1</sup> (Current Density, A g <sup>-1</sup> )	Capacity Retention, (Number of Cycles and Current, A g <sup>-1</sup> )	ΔE, V	Ref.
V <sub>2</sub> O <sub>5</sub> @PEDOT	one-pot self-polymerization at room temperature	monolithic grains/9.86	3 M Zn(CF <sub>3</sub> SO <sub>3</sub> ) <sub>2</sub>	360 (1); 280 (5); 197 (10)	~77% (4500, 10)	0.2–1.6	[57]
PEDOT/V <sub>2</sub> O <sub>5</sub>	synthesis at room temperature	2D sheet sponge/15.77	3 M ZnSO <sub>4</sub> saturated with V <sub>2</sub> O <sub>5</sub>	247 (0.2); 154 (50)	88% (700, 5)	0.2–1.6	[98]
PEDOT-VO	hydrothermal method	3D flower structure/13.95	3 M Zn(CF <sub>3</sub> SO <sub>3</sub> ) <sub>2</sub>	370.5 (0.5); ~290 (5); 175 (50)	96.9% (1000, 5)	0.2–1.4	[65]
PEDOT-V <sub>2</sub> O <sub>5</sub>	synthesis at room temperature	nanobelts/9.7	3 M Zn(CF <sub>3</sub> SO <sub>3</sub> ) <sub>2</sub>	449 (0.2); 358 (10)	94.3% (6000, 10)	0.3–1.6	[89]
V <sub>2</sub> O <sub>5</sub> @PEDOT/CC	electrodeposition	nanosheet array of core-shell particles	2.5 M Zn(CF <sub>3</sub> SO <sub>3</sub> ) <sub>2</sub>	360 (0.1); 254 (5); 232 (20)	89% (1000, 5)	0.2–1.6	[70]
V <sub>2</sub> O <sub>5</sub> ·3H <sub>2</sub> O/PEDOT: PSS	one-step hydrothermal reaction	wrinkled layers/12.9	3 M Zn(CF <sub>3</sub> SO <sub>3</sub> ) <sub>2</sub>	424 (0.2); 174 (10)	89.4% (2000, 5)	0.3–1.6	[92]
PVO/PEDOT/CNTs	wet ball-milling	nanoflakes/10.0	3 M Zn(CF <sub>3</sub> SO <sub>3</sub> ) <sub>2</sub>	440.6 (0.5); 180.0 (30)	92% (2000, 30)	0.2–1.6	[97]
VO <sub>2</sub> /PEDOT	hydrothermal method	ultrathin nanobelts/2.05	3 M Zn(CF <sub>3</sub> SO <sub>3</sub> ) <sub>2</sub>	540 (0.05); 430.4 (1); 231.2 (10)	84.5% (1000, 5)	0.3–1.3	[99]
PEDOT-NH <sub>4</sub> V <sub>3</sub> O <sub>8</sub>	sonochemical synthesis	nanofiber/11.2	2.5 M Zn(CF <sub>3</sub> SO <sub>3</sub> ) <sub>2</sub>	344 (0.5); 155 (20)	94% (1000, 10)	0.2–1.8	[58]
PEDOT-NH <sub>4</sub> V <sub>3</sub> O <sub>8</sub>	hydrothermal process, intercalation	nanobelts/10.8	3 M Zn(CF <sub>3</sub> SO <sub>3</sub> ) <sub>2</sub>	357 (0.05); 163.6 (10)	94.1% (5000, 10)	0.4–1.6	[87]
Na <sub>0.76</sub> V <sub>6</sub> O <sub>15</sub> /PEDOT	vapor polymerization	nanocables	3 M Zn(CF <sub>3</sub> SO <sub>3</sub> ) <sub>2</sub>	355 (0.05); 256 (0.1); 165 (4)	99% (2600, 4)	0.3–1.5	[100]

However, the further development of more technological/easy and reliable methods of modification of electrode materials and optimization of compositions should be investigated for practical application in the battery industry. Among the challenges going forward are the choice of appropriate guest molecules/ions allowing the functional stability during the consecutive charge–discharge cycling, and an optimization of the amount of guest modifiers providing a good balance between improved energy storage properties and cycling stability. We believe that this review would stimulate researchers for the development of such materials.

**Author Contributions:** Conceptualization, E.G.T. and V.V.K.; writing—original draft preparation, E.G.T. and V.V.K.; writing—review and editing, E.G.T. and M.A.K.; visualization, E.G.T. and M.A.K.; funding acquisition, V.V.K. All authors have read and agreed to the published version of the manuscript.

**Funding:** This research was funded by the Russian Foundation for Basic Research, grant number 21-53-53012.

**Conflicts of Interest:** The authors declare no conflict of interest.

## References

- Tian, Y.; Zeng, G.; Rutt, A.; Shi, T.; Kim, H.; Wang, J.; Koettgen, J.; Sun, Y.; Ouyang, B.; Chen, T.; et al. Promises and Challenges of Next-Generation “beyond Li-Ion” Batteries for Electric Vehicles and Grid Decarbonization. *Chem. Rev.* **2021**, *121*, 1623–1669. [[CrossRef](#)] [[PubMed](#)]
- Kubota, K.; Dahbi, M.; Hosaka, T.; Kumakura, S.; Komaba, S. Towards K-Ion and Na-Ion Batteries as “Beyond Li-Ion”. *Chem. Rec.* **2018**, *18*, 459–479. [[CrossRef](#)] [[PubMed](#)]
- Liang, Y.; Dong, H.; Aurbach, D.; Yao, Y. Current Status and Future Directions of Multivalent Metal-Ion Batteries. *Nat. Energy* **2020**, *5*, 646–656. [[CrossRef](#)]
- Biemolt, J.; Jungbacker, P.; van Teijlingen, T.; Yan, N.; Rothenberg, G. Beyond Lithium-Based Batteries. *Materials* **2020**, *13*, 425. [[CrossRef](#)] [[PubMed](#)]

5. Liu, H.; Wang, J.G.; You, Z.; Wei, C.; Kang, F.; Wei, B. Rechargeable Aqueous Zinc-Ion Batteries: Mechanism, Design Strategies and Future Perspectives. *Mater. Today* **2021**, *42*, 73–98. [[CrossRef](#)]
6. Zhang, X.; Wang, L.; Fu, H. Recent Advances in Rechargeable Zn-Based Batteries. *J. Power Sources* **2021**, *493*, 229677. [[CrossRef](#)]
7. Tang, B.; Shan, L.; Liang, S.; Zhou, J. Issues and Opportunities Facing Aqueous Zinc-Ion Batteries. *Energy Environ. Sci.* **2019**, *12*, 3288–3304. [[CrossRef](#)]
8. Ruan, P.; Xu, X.; Feng, J.; Yu, L.; Gao, X.; Shi, W.; Wu, F.; Liu, W.; Zang, X.; Ma, F.; et al. Boosting Zinc Storage Performance via Conductive Materials. *Mater. Res. Bull.* **2021**, *133*, 111077. [[CrossRef](#)]
9. Zhou, J.; Shan, L.; Wu, Z.; Guo, X.; Fang, G.; Liang, S. Investigation of V<sub>2</sub>O<sub>5</sub> as a Low-Cost Rechargeable Aqueous Zinc Ion Battery Cathode. *Chem. Commun.* **2018**, *54*, 4457–4460. [[CrossRef](#)]
10. Yan, M.; He, P.; Chen, Y.; Wang, S.; Wei, Q.; Zhao, K.; Xu, X.; An, Q.; Shuang, Y.; Shao, Y.; et al. Water-Lubricated Intercalation in V<sub>2</sub>O<sub>5</sub>·nH<sub>2</sub>O for High-Capacity and High-Rate Aqueous Rechargeable Zinc Batteries. *Adv. Mater.* **2018**, *30*, 1703725. [[CrossRef](#)]
11. Zhang, N.; Jia, M.; Dong, Y.; Wang, Y.; Xu, J.; Liu, Y.; Jiao, L.; Cheng, F. Hydrated Layered Vanadium Oxide as a Highly Reversible Cathode for Rechargeable Aqueous Zinc Batteries. *Adv. Funct. Mater.* **2019**, *29*, 1807331. [[CrossRef](#)]
12. Lai, J.; Zhu, H.; Zhu, X.; Koritala, H.; Wang, Y. Interlayer-Expanded V<sub>6</sub>O<sub>13</sub>·nH<sub>2</sub>O Architecture Constructed for an Advanced Rechargeable Aqueous Zinc-Ion Battery. *ACS Appl. Energy Mater.* **2019**, *2*, 1988–1996. [[CrossRef](#)]
13. Wang, L.; Huang, K.-W.; Chen, J.; Zheng, J. Ultralong Cycle Stability of Aqueous Zinc-Ion Batteries with Zinc Vanadium Oxide Cathodes. *Sci. Adv.* **2019**, *5*, aax4279. [[CrossRef](#)] [[PubMed](#)]
14. Li, Z.; Ren, Y.; Mo, L.; Liu, C.; Hsu, K.; Ding, Y.; Zhang, X.; Li, X.; Hu, L.; Ji, D.; et al. Impacts of Oxygen Vacancies on Zinc Ion Intercalation in VO<sub>2</sub>. *ACS Nano* **2020**, *14*, 5581–5589. [[CrossRef](#)]
15. Liu, S.; Kang, L.; Kim, J.M.; Chun, Y.T.; Zhang, J.; Jun, S.C. Recent Advances in Vanadium-Based Aqueous Rechargeable Zinc-Ion Batteries. *Adv. Energy Mater.* **2020**, *10*, 2000477. [[CrossRef](#)]
16. Liu, Y.; Hu, P.; Liu, H.; Wu, X.; Zhi, C. Tetragonal VO<sub>2</sub> Hollow Nanospheres as Robust Cathode Material for Aqueous Zinc Ion Batteries. *Mater. Today Energy* **2020**, *17*, 100431. [[CrossRef](#)]
17. Wang, W.; Yang, C.; Chi, X.; Liu, J.; Wen, B.; Liu, Y. Ultralow-Water-Activity Electrolyte Endows Vanadium-Based Zinc-Ion Batteries with Durable Lifespan Exceeding 30,000 Cycles. *Energy Storage Mater.* **2022**, *53*, 774–782. [[CrossRef](#)]
18. Li, R.; Zhang, H.; Zheng, Q.; Li, X. Porous V<sub>2</sub>O<sub>5</sub> Yolk-Shell Microspheres for Zinc Ion Battery Cathodes: Activation Responsible for Enhanced Capacity and Rate Performance. *J. Mater. Chem. A* **2020**, *8*, 5186–5193. [[CrossRef](#)]
19. Yang, Y.; Tang, Y.; Liang, S.; Wu, Z.; Fang, G.; Cao, X.; Wang, C.; Lin, T.; Pan, A.; Zhou, J. Transition Metal Ion-Preintercalated V<sub>2</sub>O<sub>5</sub> as High-Performance Aqueous Zinc-Ion Battery Cathode with Broad Temperature Adaptability. *Nano Energy* **2019**, *61*, 617–625. [[CrossRef](#)]
20. Wu, Y.; Song, T.Y.; Chen, L.N. A Review on Recent Developments of Vanadium-Based Cathode for Rechargeable Zinc-Ion Batteries. *Tungsten* **2021**, *3*, 289–304. [[CrossRef](#)]
21. He, P.; Chen, Q.; Yan, M.; Xu, X.; Zhou, L.; Mai, L.; Nan, C.-W. Building Better Zinc-Ion Batteries: A Materials Perspective. *EnergyChem* **2019**, *1*, 100022. [[CrossRef](#)]
22. Islam, S.; Lakshmi, G.B.V.S.; Siddiqui, A.M.; Husain, M.; Zulfeqar, M. Synthesis, Electrical Conductivity, and Dielectric Behavior of Polyaniline/V<sub>2</sub>O<sub>5</sub> Composites. *Int. J. Polym. Sci.* **2013**, *2013*, 307525. [[CrossRef](#)]
23. Kim, T.; Kim, H.; You, T.S.; Kim, J. Carbon-Coated V<sub>2</sub>O<sub>5</sub> Nanoparticles Derived from Metal-Organic Frameworks as a Cathode Material for Rechargeable Lithium-Ion Batteries. *J. Alloys Compd.* **2017**, *727*, 522–530. [[CrossRef](#)]
24. Qin, H.; Chen, L.; Wang, L.; Chen, X.; Yang, Z. V<sub>2</sub>O<sub>5</sub> Hollow Spheres as High Rate and Long Life Cathode for Aqueous Rechargeable Zinc Ion Batteries. *Electrochim. Acta* **2019**, *306*, 307–316. [[CrossRef](#)]
25. Chen, H.; Qin, H.; Chen, L.; Wu, J.; Yang, Z. V<sub>2</sub>O<sub>5</sub>@CNTs as Cathode of Aqueous Zinc Ion Battery with High Rate and High Stability. *J. Alloys Compd.* **2020**, *842*, 155912. [[CrossRef](#)]
26. Zhang, H.; Liu, X.; Li, H.; Qin, B.; Passerini, S. High-Voltage Operation of a V<sub>2</sub>O<sub>5</sub> Cathode in a Concentrated Gel Polymer Electrolyte for High-Energy Aqueous Zinc Batteries. *ACS Appl. Mater. Interfaces* **2020**, *12*, 15305–15312. [[CrossRef](#)] [[PubMed](#)]
27. Wang, X.; Li, Y.; Wang, S.; Zhou, F.; Das, P.; Sun, C.; Zheng, S.; Wu, Z. 2D Amorphous V<sub>2</sub>O<sub>5</sub>/Graphene Heterostructures for High-Safety Aqueous Zn-Ion Batteries with Unprecedented Capacity and Ultrahigh Rate Capability. *Adv. Energy Mater.* **2020**, *10*, 2000081. [[CrossRef](#)]
28. Javed, M.S.; Lei, H.; Wang, Z.; Liu, B.T.; Cai, X.; Mai, W. 2D V<sub>2</sub>O<sub>5</sub> Nanosheets as a Binder-Free High-Energy Cathode for Ultrafast Aqueous and Flexible Zn-Ion Batteries. *Nano Energy* **2020**, *70*, 104573. [[CrossRef](#)]
29. Zhang, W.; Zuo, C.; Tang, C.; Tang, W.; Lan, B.; Fu, X.; Dong, S.; Luo, P. The Current Developments and Perspectives of V<sub>2</sub>O<sub>5</sub> as Cathode for Rechargeable Aqueous Zinc-Ion Batteries. *Energy Technol.* **2021**, *9*, 2000789. [[CrossRef](#)]
30. Liu, Y.; Wu, X. Review of Vanadium-Based Electrode Materials for Rechargeable Aqueous Zinc Ion Batteries. *J. Energy Chem.* **2021**, *56*, 223–237. [[CrossRef](#)]
31. Yang, G.; Li, Q.; Ma, K.; Hong, C.; Wang, C. The Degradation Mechanism of Vanadium Oxide-Based Aqueous Zinc-Ion Batteries. *J. Mater. Chem. A* **2020**, *8*, 8084–8095. [[CrossRef](#)]
32. Wang, X.; Zhang, Z.; Xi, B.; Chen, W.; Jia, Y.; Feng, J.; Xiong, S. Advances and Perspectives of Cathode Storage Chemistry in Aqueous Zinc-Ion Batteries. *ACS Nano* **2021**, *15*, 9244–9272. [[CrossRef](#)] [[PubMed](#)]
33. Khairy, M.; Tinet, D.; Van Damme, H. The Synthesis of Pillared Vanadium Oxide. *J. Chem. Soc. Chem. Commun.* **1990**, 856–857. [[CrossRef](#)]

34. Jo, J.H.; Sun, Y.K.; Myung, S.T. Hollandite-Type Al-Doped VO<sub>1.52</sub>(OH)<sub>0.77</sub> as a Zinc Ion Insertion Host Material. *J. Mater. Chem. A* **2017**, *5*, 8367–8375. [[CrossRef](#)]
35. Liu, X.; Zhang, H.; Geiger, D.; Han, J.; Varzi, A.; Kaiser, U.; Moretti, A.; Passerini, S. Calcium Vanadate Sub-Microfibers as Highly Reversible Host Cathode Material for Aqueous Zinc-Ion Batteries. *Chem. Commun.* **2019**, *55*, 2265–2268. [[CrossRef](#)] [[PubMed](#)]
36. Zhao, H.; Fu, Q.; Yang, D.; Sarapulova, A.; Pang, Q.; Meng, Y.; Wei, L.; Ehrenberg, H.; Wei, Y.; Wang, C.; et al. In Operando Synchrotron Studies of NH<sub>4</sub><sup>+</sup> Preintercalated V<sub>2</sub>O<sub>5</sub>·nH<sub>2</sub>O Nanobelts as the Cathode Material for Aqueous Rechargeable Zinc Batteries. *ACS Nano* **2020**, *14*, 11809–11820. [[CrossRef](#)]
37. Zhang, Y.; Zhao, L.; Chen, A.; Sun, J. Cr<sup>3+</sup> Pre-Intercalated Hydrated Vanadium Oxide as an Excellent Performance Cathode for Aqueous Zinc-Ion Batteries. *Fundam. Res.* **2021**, *1*, 418–424. [[CrossRef](#)]
38. Kondratiev, V.V.; Holze, R. Intrinsically Conducting Polymers and Their Combinations with Redox-Active Molecules for Rechargeable Battery Electrodes: An Update. *Chem. Pap.* **2021**, *75*, 4981–5007. [[CrossRef](#)]
39. Dong, R.; Zhang, T.; Liu, J.; Li, H.; Hu, D.; Liu, X.; Xu, Q. Mechanistic Insight into Polypyrrole Coating on V<sub>2</sub>O<sub>5</sub> Cathode for Aqueous Zinc-Ion Battery. *ChemElectroChem* **2022**, *9*, 202101441. [[CrossRef](#)]
40. He, P.; Chen, S. Cathode Strategies to Improve the Performance of Zinc-ion Batteries. *Electrochem. Sci. Adv.* **2022**, *2*, 202100090. [[CrossRef](#)]
41. Jia, X.; Liu, C.; Neale, Z.G.; Yang, J.; Cao, G. Active Materials for Aqueous Zinc Ion Batteries: Synthesis, Crystal Structure, Morphology, and Electrochemistry. *Chem. Rev.* **2020**, *120*, 7795–7866. [[CrossRef](#)] [[PubMed](#)]
42. Zeng, X.; Hao, J.; Wang, Z.; Mao, J.; Guo, Z. Recent Progress and Perspectives on Aqueous Zn-Based Rechargeable Batteries with Mild Aqueous Electrolytes. *Energy Storage Mater.* **2019**, *20*, 410–437. [[CrossRef](#)]
43. Zhang, N.; Chen, X.; Yu, M.; Niu, Z.; Cheng, F.; Chen, J. Materials Chemistry for Rechargeable Zinc-Ion Batteries. *Chem. Soc. Rev.* **2020**, *49*, 4203–4219. [[CrossRef](#)] [[PubMed](#)]
44. Chen, D.; Lu, M.; Cai, D.; Yang, H.; Han, W. Recent Advances in Energy Storage Mechanism of Aqueous Zinc-Ion Batteries. *J. Energy Chem.* **2021**, *54*, 712–726. [[CrossRef](#)]
45. Chen, X.; Zhang, H.; Liu, J.-H.; Gao, Y.; Cao, X.; Zhan, C.; Wang, Y.; Wang, S.; Chou, S.-L.; Dou, S.-X.; et al. Vanadium-Based Cathodes for Aqueous Zinc-Ion Batteries: Mechanism, Design Strategies and Challenges. *Energy Storage Mater.* **2022**, *50*, 21–46. [[CrossRef](#)]
46. Pam, M.E.; Yan, D.; Yu, J.; Fang, D.; Guo, L.; Li, X.L.; Li, T.C.; Lu, X.; Ang, L.K.; Amal, R.; et al. Microstructural Engineering of Cathode Materials for Advanced Zinc-Ion Aqueous Batteries. *Adv. Sci.* **2021**, *8*, 2002722. [[CrossRef](#)] [[PubMed](#)]
47. Liu, Z.; Sun, H.; Qin, L.; Cao, X.; Zhou, J.; Pan, A.; Fang, G.; Liang, S. Interlayer Doping in Layered Vanadium Oxides for Low-cost Energy Storage: Sodium-ion Batteries and Aqueous Zinc-ion Batteries. *ChemNanoMat* **2020**, *6*, 1553–1566. [[CrossRef](#)]
48. Karapidakis, E.; Vernardou, D. Progress on V<sub>2</sub>O<sub>5</sub> Cathodes for Multivalent Aqueous Batteries. *Materials* **2021**, *14*, 2310. [[CrossRef](#)]
49. Sengodu, P.; Deshmukh, A.D. Conducting Polymers and Their Inorganic Composites for Advanced Li-Ion Batteries: A Review. *RSC Adv.* **2015**, *5*, 42109–42130. [[CrossRef](#)]
50. Eliseeva, S.N.; Kamenskii, M.A.; Tolstopjatova, E.G.; Kondratiev, V.V. Effect of Combined Conductive Polymer Binder on the Electrochemical Performance of Electrode Materials for Lithium-Ion Batteries. *Energies* **2020**, *13*, 2163. [[CrossRef](#)]
51. Nguyen, V.A.; Kuss, C. Review—Conducting Polymer-Based Binders for Lithium-Ion Batteries and Beyond. *J. Electrochem. Soc.* **2020**, *167*, 065501. [[CrossRef](#)]
52. Shin, J.; Choi, D.S.; Lee, H.J.; Jung, Y.; Choi, J.W. Hydrated Intercalation for High-Performance Aqueous Zinc Ion Batteries. *Adv. Energy Mater.* **2019**, *9*, 1900083. [[CrossRef](#)]
53. Zeng, J.; Zhang, Z.; Guo, X.; Li, G. A Conjugated Polyaniline and Water Co-Intercalation Strategy Boosting Zinc-Ion Storage Performances for Rose-like Vanadium Oxide Architectures. *J. Mater. Chem. A* **2019**, *7*, 21079–21084. [[CrossRef](#)]
54. Liu, Y.; Pan, Z.; Tian, D.; Hu, T.; Jiang, H.; Yang, J.; Sun, J.; Zheng, J.; Meng, C.; Zhang, Y. Employing “One for Two” Strategy to Design Polyaniline-Intercalated Hydrated Vanadium Oxide with Expanded Interlayer Spacing for High-Performance Aqueous Zinc-Ion Batteries. *Chem. Eng. J.* **2020**, *399*, 125842. [[CrossRef](#)]
55. Guan, X.; Sun, Q.; Sun, C.; Duan, T.; Nie, W.; Liu, Y.; Zhao, K.; Cheng, H.; Lu, X. Tremella-like Hydrated Vanadium Oxide Cathode with an Architectural Design Strategy toward Ultralong Lifespan Aqueous Zinc-Ion Batteries. *ACS Appl. Mater. Interfaces* **2021**, *13*, 41688–41697. [[CrossRef](#)]
56. Gu, Y.; Han, Y.; Qin, Z.; Li, D.; Wang, L. A Strategy to Control Crystal Water Content in Hydrated Vanadium Oxide Cathode for Promoting Aqueous Rechargeable Zinc-Ion Batteries. *J. Alloys Compd.* **2022**, *911*, 165102. [[CrossRef](#)]
57. Yao, Z.; Wu, Q.; Chen, K.; Liu, J.; Li, C. Shallow-Layer Pillaring of a Conductive Polymer in Monolithic Grains to Drive Superior Zinc Storage via a Cascading Effect. *Energy Environ. Sci.* **2020**, *13*, 3149–3163. [[CrossRef](#)]
58. Kim, J.; Lee, S.H.; Park, C.; Kim, H.; Park, J.; Chung, K.Y.; Ahn, H. Controlling Vanadate Nanofiber Interlayer via Intercalation with Conducting Polymers: Cathode Material Design for Rechargeable Aqueous Zinc Ion Batteries. *Adv. Funct. Mater.* **2021**, *31*, 2100005. [[CrossRef](#)]
59. Wu, C.G.; DeGroot, D.C.; Marcy, H.O.; Schindler, J.L.; Kannewurf, C.R.; Liu, Y.J.; Hirpo, W.; Kanatzidis, M.G. Redox Intercalative Polymerization of Aniline in V<sub>2</sub>O<sub>5</sub> Xerogel. The Postintercalative Intralamellar Polymer Growth in Polyaniline/Metal Oxide Nanocomposites Is Facilitated by Molecular Oxygen. *Chem. Mater.* **1996**, *8*, 1992–2004. [[CrossRef](#)]

60. Liu, S.; Zhu, H.; Zhang, B.; Li, G.; Zhu, H.; Ren, Y.; Geng, H.; Yang, Y.; Liu, Q.; Li, C.C. Tuning the Kinetics of Zinc-Ion Insertion/Extraction in  $V_2O_5$  by In Situ Polyaniline Intercalation Enables Improved Aqueous Zinc-Ion Storage Performance. *Adv. Mater.* **2020**, *32*, 2001113. [[CrossRef](#)]
61. Kanatzidis, M.G.; Wu, C.G.; Marcy, H.O.; Kannewurf, C.R. Conductive Polymer Bronzes. Intercalated Polyaniline in  $V_2O_5$  Xerogels. *J. Am. Chem. Soc.* **1989**, *111*, 4139–4141. [[CrossRef](#)]
62. Yin, C.; Pan, C.; Liao, X.; Pan, Y.; Yuan, L. Regulating the Interlayer Spacing of Vanadium Oxide by In Situ Polyaniline Intercalation Enables an Improved Aqueous Zinc-Ion Storage Performance. *ACS Appl. Mater. Interfaces* **2021**, *13*, 39347–39354. [[CrossRef](#)]
63. Li, R.; Xing, F.; Li, T.; Zhang, H.; Yan, J.; Zheng, Q.; Li, X. Intercalated Polyaniline in  $V_2O_5$  as a Unique Vanadium Oxide Bronze Cathode for Highly Stable Aqueous Zinc Ion Battery. *Energy Storage Mater.* **2021**, *38*, 590–598. [[CrossRef](#)]
64. Zhang, Y.; Huang, R.; Wang, X.; Wang, Z.; Song, B.; Du, Y.; Lu, Q.; Chen, X.; Sun, J. Facile Large-Scale Preparation of Vanadium Pentoxide-Polypyrrole Composite for Aqueous Zinc-Ion Batteries. *J. Alloys Compd.* **2022**, *907*, 164434. [[CrossRef](#)]
65. Li, S.; Wei, X.; Wu, C.; Zhang, B.; Wu, S.; Lin, Z. Constructing Three-Dimensional Structured  $V_2O_5$ /Conductive Polymer Composite with Fast Ion/Electron Transfer Kinetics for Aqueous Zinc-Ion Battery. *ACS Appl. Energy Mater.* **2021**, *4*, 4208–4216. [[CrossRef](#)]
66. Volkov, F.S.; Eliseeva, S.N.; Kamenskii, M.A.; Volkov, A.I.; Tolstopjatova, E.G.; Glumov, O.V.; Fu, L.; Kondratiev, V.V. Vanadium Oxide-Poly(3,4-Ethylenedioxythiophene) Nanocomposite as High-Performance Cathode for Aqueous Zn-Ion Batteries: The Structural and Electrochemical Characterization. *Nanomaterials* **2022**, *12*, 3896. [[CrossRef](#)] [[PubMed](#)]
67. Du, Y.; Wang, X.; Man, J.; Sun, J. A Novel Organic-Inorganic Hybrid  $V_2O_5$ @polyaniline as High-Performance Cathode for Aqueous Zinc-Ion Batteries. *Mater. Lett.* **2020**, *272*, 127813. [[CrossRef](#)]
68. Zhang, Z.; Xi, B.; Wang, X.; Ma, X.; Chen, W.; Feng, J.; Xiong, S. Oxygen Defects Engineering of  $VO_2 \cdot xH_2O$  Nanosheets via In Situ Polypyrrole Polymerization for Efficient Aqueous Zinc Ion Storage. *Adv. Funct. Mater.* **2021**, *31*, 2103070. [[CrossRef](#)]
69. Ling, H.; Zhang, R.; Ye, X.; Wen, Z.; Xia, J.; Lu, X. In-Situ Synthesis of Organic-Inorganic Hybrid Thin Film of PEDOT/  $V_2O_5$  as Hole Transport Layer for Polymer Solar Cells. *Sol. Energy* **2019**, *190*, 63–68. [[CrossRef](#)]
70. Xu, D.; Wang, H.; Li, F.; Guan, Z.; Wang, R.; He, B.; Gong, Y.; Hu, X. Conformal Conducting Polymer Shells on  $V_2O_5$  Nanosheet Arrays as a High-Rate and Stable Zinc-Ion Battery Cathode. *Adv. Mater. Interfaces* **2019**, *6*, 1801506. [[CrossRef](#)]
71. Huang, J.; Wang, Z.; Hou, M.; Dong, X.; Liu, Y.; Wang, Y.; Xia, Y. Polyaniline-Intercalated Manganese Dioxide Nanolayers as a High-Performance Cathode Material for an Aqueous Zinc-Ion Battery. *Nat. Commun.* **2018**, *9*, 2906. [[CrossRef](#)] [[PubMed](#)]
72. Dallas, P.; Stamopoulos, D.; Boukos, N.; Tzitzios, V.; Niarchos, D.; Petridis, D. Characterization, Magnetic and Transport Properties of Polyaniline Synthesized through Interfacial Polymerization. *Polymer* **2007**, *48*, 3162–3169. [[CrossRef](#)]
73. Li, Z.; Gong, L. Research Progress on Applications of Polyaniline (PANI) for Electrochemical Energy Storage and Conversion. *Materials* **2020**, *13*, 548. [[CrossRef](#)] [[PubMed](#)]
74. Kim, C.; Ahn, B.Y.; Wei, T.S.; Jo, Y.; Jeong, S.; Choi, Y.; Kim, I.D.; Lewis, J.A. High-Power Aqueous Zinc-Ion Batteries for Customized Electronic Devices. *ACS Nano* **2018**, *12*, 11838–11846. [[CrossRef](#)]
75. Wan, F.; Zhang, L.; Wang, X.; Bi, S.; Niu, Z.; Chen, J. An Aqueous Rechargeable Zinc-Organic Battery with Hybrid Mechanism. *Adv. Funct. Mater.* **2018**, *28*, 1804975. [[CrossRef](#)]
76. Chen, S.; Li, K.; Hui, K.S.; Zhang, J. Regulation of Lamellar Structure of Vanadium Oxide via Polyaniline Intercalation for High-Performance Aqueous Zinc-Ion Battery. *Adv. Funct. Mater.* **2020**, *30*, 2003890. [[CrossRef](#)]
77. Zhang, Y.; Xu, L.; Jiang, H.; Liu, Y.; Meng, C. Polyaniline-Expanded the Interlayer Spacing of Hydrated Vanadium Pentoxide by the Interface-Intercalation for Aqueous Rechargeable Zn-Ion Batteries. *J. Colloid Interface Sci.* **2021**, *603*, 641–650. [[CrossRef](#)]
78. Liu, Y.-J.; DeGroot, D.C.; Schindler, J.L.; Kannewurf, C.R.; Kanatzidis, M.G. Stabilization of Anilinium in Vanadium(V) Oxide Xerogel and Its Post-Intercalative Polymerization to Poly(Aniline) in Air. *J. Chem. Soc. Chem. Commun.* **1993**, 593–596. [[CrossRef](#)]
79. Li, W.; Han, C.; Gu, Q.; Chou, S.L.; Wang, J.Z.; Liu, H.K.; Dou, S.X. Electron Delocalization and Dissolution-Restraint in Vanadium Oxide Superlattices to Boost Electrochemical Performance of Aqueous Zinc-Ion Batteries. *Adv. Energy Mater.* **2020**, *10*, 2001852. [[CrossRef](#)]
80. Wang, M.; Zhang, J.; Zhang, L.; Li, J.; Wang, W.; Yang, Z.; Zhang, L.; Wang, Y.; Chen, J.; Huang, Y.; et al. Graphene-like Vanadium Oxygen Hydrate (VOH) Nanosheets Intercalated and Exfoliated by Polyaniline (PANI) for Aqueous Zinc-Ion Batteries (ZIBs). *ACS Appl. Mater. Interfaces* **2020**, *12*, 31564–31574. [[CrossRef](#)]
81. Qin, X.; Wang, X.; Sun, J.; Lu, Q.; Omar, A.; Mikhailova, D. Polypyrrole Wrapped  $V_2O_5$  Nanowires Composite for Advanced Aqueous Zinc-Ion Batteries. *Front. Energy Res.* **2020**, *8*, 199. [[CrossRef](#)]
82. Qian, T.; Xu, N.; Zhou, J.; Yang, T.; Liu, X.; Shen, X.; Liang, J.; Yan, C. Interconnected Three-Dimensional  $V_2O_5$ /Polypyrrole Network Nanostructures for High Performance Solid-State Supercapacitors. *J. Mater. Chem. A* **2015**, *3*, 488–493. [[CrossRef](#)]
83. Rapi, S.; Bocchi, V.; Gardini, G.P. Conducting Polypyrrole by Chemical Synthesis in Water. *Synth. Met.* **1988**, *24*, 217–221. [[CrossRef](#)]
84. Diaz, A.F.; Castillo, J.I.; Logan, J.A.; Lee, W.-Y. Electrochemistry of Conducting Polypyrrole Films. *J. Electroanal. Chem. Interfacial Electrochem.* **1981**, *129*, 115–132. [[CrossRef](#)]
85. Feng, Z.; Sun, J.; Liu, Y.; Jiang, H.; Hu, T.; Cui, M.; Tian, F.; Meng, C.; Zhang, Y. Polypyrrole-Intercalation Tuning Lamellar Structure of  $V_2O_5 \cdot nH_2O$  Boosts Fast Zinc-Ion Kinetics for Aqueous Zinc-Ion Battery. *J. Power Sources* **2022**, *536*, 231489. [[CrossRef](#)]
86. Wang, W.; He, D.; Fang, Y.; Wang, S.; Zhang, Z.; Zhao, R.; Xue, W. Pillaring of a Conductive Polymer in Layered  $V_2O_5$  Boosting Ultra-Fast  $Zn^{2+}/H^+$  Storage in Aqueous Media. *Electrochim. Acta* **2022**, *416*, 140270. [[CrossRef](#)]

87. Bin, D.; Huo, W.; Yuan, Y.; Huang, J.; Liu, Y.; Zhang, Y.; Dong, F.; Wang, Y.; Xia, Y. Organic-Inorganic-Induced Polymer Intercalation into Layered Composites for Aqueous Zinc-Ion Battery. *Chem* **2020**, *6*, 968–984. [[CrossRef](#)]
88. Liao, M.; Wang, J.; Ye, L.; Sun, H.; Wen, Y.; Wang, C.; Sun, X.; Wang, B.; Peng, H. A Deep-Cycle Aqueous Zinc-Ion Battery Containing an Oxygen-Deficient Vanadium Oxide Cathode. *Angew. Chemie Int. Ed.* **2020**, *59*, 2273–2278. [[CrossRef](#)]
89. Du, Y.; Wang, X.; Sun, J. Tunable Oxygen Vacancy Concentration in Vanadium Oxide as Mass-Produced Cathode for Aqueous Zinc-Ion Batteries. *Nano Res.* **2021**, *14*, 754–761. [[CrossRef](#)]
90. Heywang, G.; Jonas, F. Poly(Alkylenedioxythiophene)s—New, Very Stable Conducting Polymers. *Adv. Mater.* **1992**, *4*, 116–118. [[CrossRef](#)]
91. Petsagkourakis, I.; Kim, N.; Tybrandt, K.; Zozoulenko, I.; Crispin, X. Poly(3,4-ethylenedioxythiophene): Chemical Synthesis, Transport Properties, and Thermoelectric Devices. *Adv. Electron. Mater.* **2019**, *5*, 1800918. [[CrossRef](#)]
92. Du, Y.; Chen, Y.; Yang, M.; Zou, S.; Song, X.; Fu, Y.; Li, J.; Li, Y.; He, D. Poly(3,4-Ethylenedioxythiophene)-Polystyrenesulfonate-Added Layered Vanadium Oxide Cathode for High-Performance Zinc-Ion Batteries. *ACS Appl. Energy Mater.* **2021**, *4*, 14582–14589. [[CrossRef](#)]
93. Murugan, A.V.; Kale, B.B.; Kwon, C.; Campet, G.; Vijayamohanan, K. Synthesis and Characterization of a New Organo-Inorganic Poly(3,4-Ethylene Dioxythiophene) PEDOT/ V<sub>2</sub>O<sub>5</sub> Nanocomposite by Intercalation. *J. Mater. Chem.* **2001**, *11*, 2470–2475. [[CrossRef](#)]
94. Ma, L.; Wang, X.; Sun, J. A Strategy Associated with Conductive Binder and 3D Current Collector for Aqueous Zinc-Ion Batteries with High Mass Loading. *J. Electroanal. Chem.* **2020**, *873*, 114395. [[CrossRef](#)]
95. Volkov, F.S.; Tolstopjatova, E.G.; Eliseeva, S.N.; Kamenskii, M.A.; Vypritskaia, A.I.; Volkov, A.I.; Kondratiev, V.V. Vanadium(V) Oxide Coated by Poly(3,4-Ethylenedioxythiophene) as Cathode for Aqueous Zinc-Ion Batteries with Improved Electrochemical Performance. *Mater. Lett.* **2022**, *308*, 131210. [[CrossRef](#)]
96. Liu, C.; Lu, Q.; Omar, A.; Mikhailova, D. A Facile Chemical Method Enabling Uniform Zn Deposition for Improved Aqueous Zn-Ion Batteries. *Nanomaterials* **2021**, *11*, 764. [[CrossRef](#)]
97. Liu, X.; Ni, W.; Wang, Y.; Liang, Y.; Wu, B.; Xu, G.; Wei, X.; Yang, L. Water-Processable and Multiscale-Designed Vanadium Oxide Cathodes with Predominant Zn<sup>2+</sup> Intercalation Pseudocapacitance toward High Gravimetric/Areal/Volumetric Capacity. *Small* **2022**, *18*, 2105796. [[CrossRef](#)]
98. Wang, B.; Dai, S.; Zhu, Z.; Hu, L.; Su, Z.; Jin, Y.; Xiong, L.; Gao, J.; Wan, J.; Li, Z.; et al. A Two-Dimensional Conductive Polymer/V<sub>2</sub>O<sub>5</sub> Composite with Rapid Zinc-Ion Storage Kinetics for High-Power Aqueous Zinc-Ion Batteries. *Nanoscale* **2022**, *14*, 12013–12021. [[CrossRef](#)]
99. Liu, X.; Xu, G.; Zhang, Q.; Huang, S.; Li, L.; Wei, X.; Cao, J.; Yang, L.; Chu, P.K. Ultrathin Hybrid Nanobelts of Single-Crystalline VO<sub>2</sub> and Poly(3,4-Ethylenedioxythiophene) as Cathode Materials for Aqueous Zinc Ion Batteries with Large Capacity and High-Rate Capability. *J. Power Sources* **2020**, *463*, 228223. [[CrossRef](#)]
100. Bi, W.; Gao, G.; Wu, G.; Atif, M.; AlSalhi, M.S.; Cao, G. Sodium Vanadate/PEDOT Nanocables Rich with Oxygen Vacancies for High Energy Conversion Efficiency Zinc Ion Batteries. *Energy Storage Mater.* **2021**, *40*, 209–218. [[CrossRef](#)]
101. Yan, X.; Feng, X.; Hao, B.; Liu, J.; Yu, Y.; Qi, J.; Wang, H.; Wang, Z.; Hu, Y.; Fan, X.; et al. Enhancing the Kinetics of Vanadium Oxides via Conducting Polymer and Metal Ions Co-Intercalation for High-Performance Aqueous Zinc-Ions Batteries. *J. Colloid Interface Sci.* **2022**, *628*, 204–213. [[CrossRef](#)] [[PubMed](#)]
102. Zhang, Y.; Du, Y.; Song, B.; Wang, Z.; Wang, X.; Wan, F.; Ma, X. Manganese-Ions and Polyaniline Co-Intercalation into Vanadium Oxide for Stable Zinc-Ion Batteries. *J. Power Sources* **2022**, *545*, 231920. [[CrossRef](#)]
103. Feng, Z.; Zhang, Y.; Zhao, Y.; Sun, J.; Liu, Y.; Jiang, H.; Cui, M.; Hu, T.; Meng, C. Dual Intercalation of Inorganics–Organics for Synergistically Tuning the Layer Spacing of V<sub>2</sub>O<sub>5</sub>·nH<sub>2</sub>O to Boost Zn<sup>2+</sup> Storage for Aqueous Zinc-Ion Batteries. *Nanoscale* **2022**, *14*, 8776–8788. [[CrossRef](#)] [[PubMed](#)]
104. Yan, H.; Ru, Q.; Gao, P.; Shi, Z.; Gao, Y.; Chen, F.; Chi-Chun Ling, F.; Wei, L. Organic Pillars Pre-Intercalated V<sup>4+</sup>-V<sub>2</sub>O<sub>5</sub>·3H<sub>2</sub>O Nanocomposites with Enlarged Interlayer and Mixed Valence for Aqueous Zn-Ion Storage. *Appl. Surf. Sci.* **2020**, *534*, 147608. [[CrossRef](#)]
105. Li, Y.; Liu, Y.; Chen, J.; Zheng, Q.; Huo, Y.; Xie, F.; Lin, D. Polyaniline Intercalation Induced Great Enhancement of Electrochemical Properties in Ammonium Vanadate Nanosheets as an Advanced Cathode for High-Performance Aqueous Zinc-Ion Batteries. *Chem. Eng. J.* **2022**, *448*, 137681. [[CrossRef](#)]
106. Wang, Z.; Tang, X.; Yuan, S.; Bai, M.; Wang, H.; Liu, S.; Zhang, M.; Ma, Y. Engineering Vanadium Pentoxide Cathode for the Zero-Strain Cation Storage via a Scalable Intercalation-Polymerization Approach. *Adv. Funct. Mater.* **2021**, *31*, 2100164. [[CrossRef](#)]